Coordination Chemistry Reviews 391 (2019) 15–29

Contents lists available at ScienceDirect

Coordination Chemistry Reviews

journal homepage: www.elsevier.com/locate/ccr

Review

Mechanical properties of hybrid organic-inorganic perovskites

Li-Jun Ji [a,b], Shi-Jing Sun [c,*], Yan Qin [b], Kai Li [a], Wei Li [a,d,e,*]

[a] School of Materials Science and Engineering & National Institute for Advanced Materials, Nankai University, Tianjin 300350, China
[b] School of Physics & Wuhan National Laboratory for Optoelectronics, Huazhong University of Science and Technology, Wuhan 430074, China
[c] Department of Mechanical Engineering, Massachusetts Institute of Technology, MA 02139, United States
[d] Hubei Key Laboratory of Optical Information and Pattern Recognition, Wuhan Institute of Technology, Wuhan 430205, China
[e] School of Physics and Electronic Engineering, Xinyang Normal University, Xinyang 464000, China

ARTICLE INFO

Article history:
Received 10 January 2019
Received in revised form 21 March 2019
Accepted 30 March 2019
Available online 15 April 2019

Keywords:
Hybrid organic-inorganic perovskites
Mechanical property
Structure-property relationship
Perovskite thin-films
Strain engineering

ABSTRACT

Hybrid organic-inorganic perovskites (HOIPs) have attracted significant attention in recent years attributed to their outstanding physical properties and striking application potentials in the fields of photovoltaic and optoelectronic devices. For the commercialization of devices employing hybrid perovskite materials, their mechanical properties critically influence the manufacturing, processing as well as the device durability, and hence need to be well understood. In this review, we summarize recent mechanical studies of the known HOIPs. Firstly, we present a comprehensive account of the relationship between crystal structures and properties, where the influence of different chemical and bonding factors on the load response of HOIPs are extensively discussed. The functional abnormalities of HOIP materials under the stress stimuli are also reviewed, addressing the effects of negative linear compressibility, negative Poisson's ratio and barocaloric effect. Finally, we briefly summarize the significant effect of strain and stress in thin-film halide perovskite materials, which have been widely employed in solar cells and Light-emitting diodes. This review aims to raise more awareness about the fundamental understanding of the mechanical properties of hybrid perovskite materials, and attract more research attention to this interdisciplinary field.

Contents

* Corresponding authors at: School of Materials Science and Engineering & National Institute for Advanced Materials, Nankai University, Tianjin 300350, China (W. Li).
E-mail addresses: shijings@mit.edu (S.-J. Sun), wl276@nankai.edu.cn (W. Li).

https://doi.org/10.1016/j.ccr.2019.03.020
0010-8545/

1. Introduction

Since the discovery of the first perovskite mineral, $CaTiO_3$ almost a century ago, materials with perovskite structure have played an important role in a wide range of applications, such as ferroelectrics, catalysis and more recently, in photovoltaics [1]. A conventional perovskite structure consists of an ABX_3 framework, where the BX_6 octahedra form a corner-sharing three-dimensional network and the A-site cations sit in the cuboctahedral cavity. Hybrid organic-inorganic perovskites (HOIPs) is a sub-class of the perovskite family, where the inorganic A, B and/or X-sites are replaced by organic ions [2,3]. For example, in $CH_3NH_3PbI_3$, a monovalent organic amine and a divalent metal cation sit on A and B-site, respectively [4], whereas in $(CH_3NH_3)[Mn(CHOO)_3]$, ionic molecule groups occupy both A and X-sites [5]. Goldschmidt tolerance factor has been used to access the structural stability of perovskite architecture for decades [6] and it has been recently adapted to HOIPs with estimations on the size of organic cations as spheres or cylinders according to their shapes [7–10].

The introduction of organic components in perovskite architectures enables enormous structural and chemical possibilities, and hence HOIPs exhibit tunable functionality and a wide range of mechanical properties that are unachievable in purely inorganic perovskite [3]. For example, HOIP-based semiconductors have revolutionized the thin-film photovoltaic technology in the past a few years [11]. The application of HOIPs in flexible solar cells is attributed to the high degrees of flexibility in response to a mechanical perturbation in hybrid halide perovskites [12]. More recently, the stress-stimulated functions such as piezoelectric responses and barocaloric effects were also found in HOIPs, extending their functionalities to a broader horizon [13,14]. Given these promising features, the complex structural-mechanical property relationships of HOIPs have attracted increasing attention since they are critical factors which determine materials' long term stability and reliability in service [15–17]. Nevertheless, the majority of published work focused on the synthesis of novel HOIP structures and demonstration of optoelectronic functionalities, only a small amount of studies devoted to the understanding of the mechanical behavior of HOIPs. The experimental and theoretical studies of HOIPs' deformation mechanisms were mainly on the halide perovskites. Feng [18] was among the first to use density functional theory (DFT) to calculate the elastic moduli of $CH_3NH_3MX_3$ (M = Sn, Pb; X = Br, I). Cheetham et al. and Cahen et al. provided experimental microscopic insight in the structure-determined flexibility of bulk $CH_3NH_3PbX_3$ (X = Cl, Br and I) single crystals [19–22]. Lomonosov et al. measured the elastic constants of $CH_3NH_3PbBr_3$ by laser ultrasonics technology and found that both the low shear rigidity and high elastic anisotropy of the HOIP were unexpected extreme than the theoretically calculated results [23]. Létoublon et al. and Ferreira et al. conducted neutron, Brillouin and ultrasound scatterings to quantify the sound velocities of $CH_3NH_3PbX_3$ (X = I and Br), $[(NH_2)_2CH]PbBr_3$ and a-$[(NH_2)_2CH]PbI_3$ single crystal which can convert into elastic constants [24,25]. Mante and co-workers demonstrated that the directional negative thermal expansion of $CH_3NH_3PbI_3$ was resulted from the strong coherent shear phonon generation [26]. Outside the field of halide perovskites, Gao [27,28] and Goodwin [29] investigated the anomalous thermal expansion of formate hybrid perovskites via X-ray crystallography. Inspired by above pioneers, nanoindentation [30], high-pressure crystallography [31], density functional theory (DFT) calculations [32–34] and other techniques have nowadays become more commonly used tools to quantify the mechanical metrics of HOIPs [25,35].

In this review, we first focus on structure-property relationships and discuss how different chemical and structural factors influence the mechanical properties of HOIPs. The significant mechanical diversities of HOIPs arise from the discrete bonding modes and orbital states enabled by different A-, B-, and X-sites. We then review the latest understanding of the mechanism of abnormal mechanical behaviors of HOIPs, in which the load or pressure is responsible for these predicted performances. In particular, we summarize the recent investigations about negative linear compressibility, negative Poisson's ratio, and barocaloric effect. Finally, we briefly discuss the importance of mechanical properties of perovskite thin films widely used in solar cells and other devices.

2. Structure-property relationships

Understanding the structure and mechanical property relationship [39] in HOIP materials is critical for rational materials design with tailored mechanical properties. Stiffness and softness of known hybrid perovskites can be reflected by conventional mechanical metrics such as Young's modulus (E) and hardness (H). We plot the reported and recently acquired data of E and H of HOIPs including formates, halides, dicyanamides, hypophosphites, and azides, as well as perovskite oxides in Fig. 1 to give a brief overview of the distribution of E and H.

The flexibility of a hybrid perovskite is usually attributed to the framework's deformability, which is evident in phenomena such as pressure-induced amorphization [39]. However, in some cases, mechanical performances are also strongly influenced by host-guest interactions and orbital effects [40]. The purpose of this section is to facilitate the understanding of mechanical behaviors in terms of different structural components. For most hybrid perovskites, these influencing factors are coupled together in a cooperative manner.

2.1. Effects of the A-site organic amine cations: hydrogen bonding

Li et al. first reported the significant difference in mechanical properties (up to a factor of two) between two formate HOIPs,

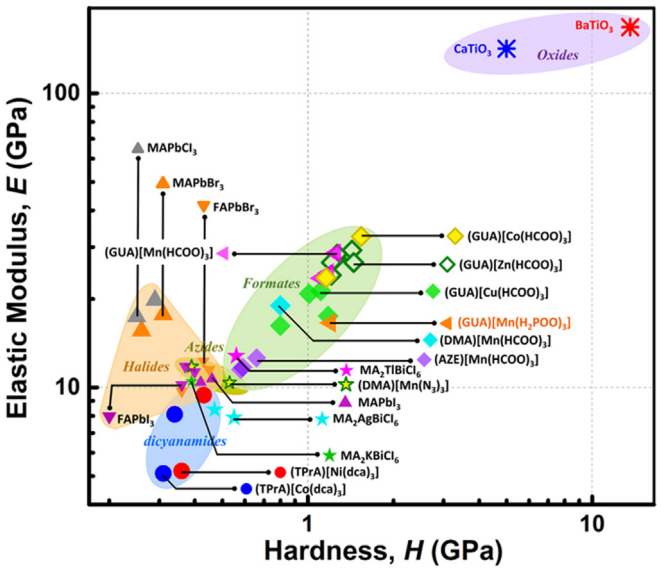

Fig. 1. Overview of elastic moduli (E) *Vs* hardness (H) plots of HOIPs and several well-known perovskite oxides (x and y-axes are in log scale). Among these HOIPs, E and H lie in the ranges of about 5–30 GPa and 0.2–1.3 GPa, respectively. Data of $(GUA)[Mn(H_2PO_2)_3]$, $(DMA)[Mn(N_3)_3]$, $(TPrA)[Co(dca)_3]$ and $(TPrA)[Ni(dca)_3]$ were added from unpublished work (Ref. [36]). Formates seem to be more rigid than hypophosphites, azides, and dicyanometallates. Comparing with inorganic perovskite oxides, such as $BaTiO_3$ ($E \approx 167.9$ GPa and $H \approx 13.6$ GPa, Ref. [37]) and $CaTiO_3$ ($E \approx 142$ GPa and $H \approx 5$ GPa, Ref. [38]), HOIPs are much softer and possess more excellent flexibility.

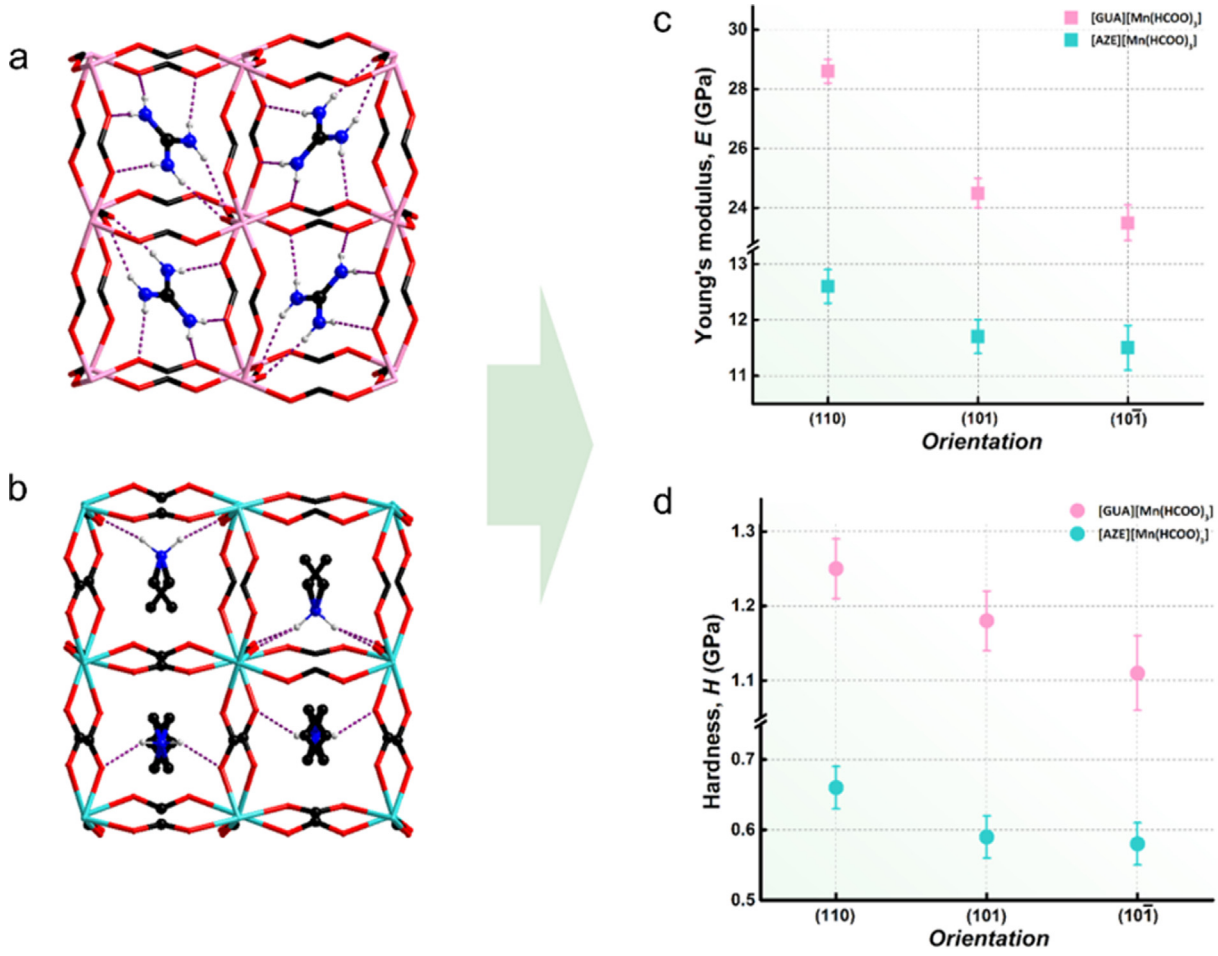

Fig. 2. Structural diagram of (a) (GUA)[Mn(HCOO)$_3$] (GUA-1) and (b) (AZE)[Mn(HCOO)$_3$] (AZE-2) viewed along the (10$\bar{1}$) direction. Only H atoms bonded with N atoms are shown for demonstration, and the N–H···O hydrogen bonds are represented as dashed lines. Color scheme: Mn, rose or aqua; N, blue; C, black; H, light gray. (c) Elastic modulus (*E*) and (d) hardness (*H*) values of GUA-1 and AZE-2. The error bars represent the standard deviations of 10–20 measurements made on each facet.

(GUA)[Mn(HCOO)$_3$] (GUA-1, GUA = guanidinium) (Fig. 2a), and (AZE)[Mn(HCOO)$_3$] (AZE-2, AZE = azetidinium) (Fig. 2b). While GUA-1 and AZE-2 crystallize in different orthorhombic space groups with comparable cell parameters [41], such difference in their mechanical performance was attributed to their distinct modes of hydrogen bonding between the A-site amine cations and the [Mn(HCOO)$_3$]$^-$ framework host.

As shown in Fig. 2, nanoindentation measurements were performed on the (10$\bar{1}$) planes of GUA-1 and AZE-2, respectively. The elastic moduli of GUA-1 (24–29 GPa) are about twice as those of AZE-2 (12–13 GPa) along the same indentation direction (Fig. 2c). Both the two perovskites crystallize in an orthorhombic symmetry and are only slightly different in density (GUA-1 is about 3.3% denser than AZE-2), the latter is expected to contribute infinitesimally on their utterly different mechanical responses. Each GUA$^+$ ([(NH$_2$)$_3$C]$^+$) in GUA-1 is tilted from (10$\bar{1}$) plane and cross-links two perpendicular edges of each pseudocubic unit cell by six N–H···O bonds, leading to strong bonding in three orthogonal directions (Fig. 2a). By contrast, the AZE$^+$ ([(CH$_2$)$_3$NH$_2$]$^+$) cations in AZE-2 arrange bonds to two edges of the pseudocubic unit cell by four hydrogen bonds (Fig. 2b), giving a few cross-linked bonding only on one of the pseudocubic unit cell face. Hence, the GUA$^+$ ions in GUA-1 are constrained tighter by the [Mn(HCOO)$_3$]$^-$ host and can resist much larger mechanical deformation, leading to higher elastic modulus (Fig. 2c) and hardness (Fig. 2d). Furthering DFT calculations indicate that the hydrogen-bonding energy of GUA-1 (ca. −4.63 eV) is about 55% greater than that in AZE-2 (ca. −3.01 eV). High-pressure and variable temperature single crystal X-ray results have drawn the same conclusions.

It is worth noting that the diverse sizes of A-site cations (about 15% difference between the size of GUA$^+$ and AZE$^+$) did not show significant effects on the elastic moduli. A similar phenomenon has also been observed in halide HOIPs. Kieslich and co-workers reported that the effective radius of MA$^+$ (MA = methylammonium) is about 16% smaller than it of FA$^+$ (FA = formamidinium) [8], however, the modulus of lead bromide perovskites is MA > FA [19]. In both halide and formate perovskites, the effect of A-site cation size is less significant than host-guest interaction and linker effects on mechanical flexibility. The detailed functional mechanism is reviewed in detail in Section 2.3.1.

2.2. Electronic states of the B-site

2.2.1. Jahn-Teller (JT) effect

Gui et al. [42] recently studied the influence of the JT effect on HOIP's flexibility by comparing the mechanical properties of (GUA)[Zn(HCOO)$_3$] (GUA-Zn) (Fig. 3a) with the JT active (GUA)[Cu(HCOO)$_3$] (GUA-Cu) (Fig. 3b). Both the GUA-Zn and GUA-Cu crystallize in an orthorhombic symmetry. In contrast to Zn-O bonds (range from 2.086 to 2.127 Å) (Fig. 3c), two Cu–O bonds in the considerably deformed CuO$_6$ octahedra are notably elongated, reaching to 2.360 and 2.383 Å, respectively, while the four other Cu–O

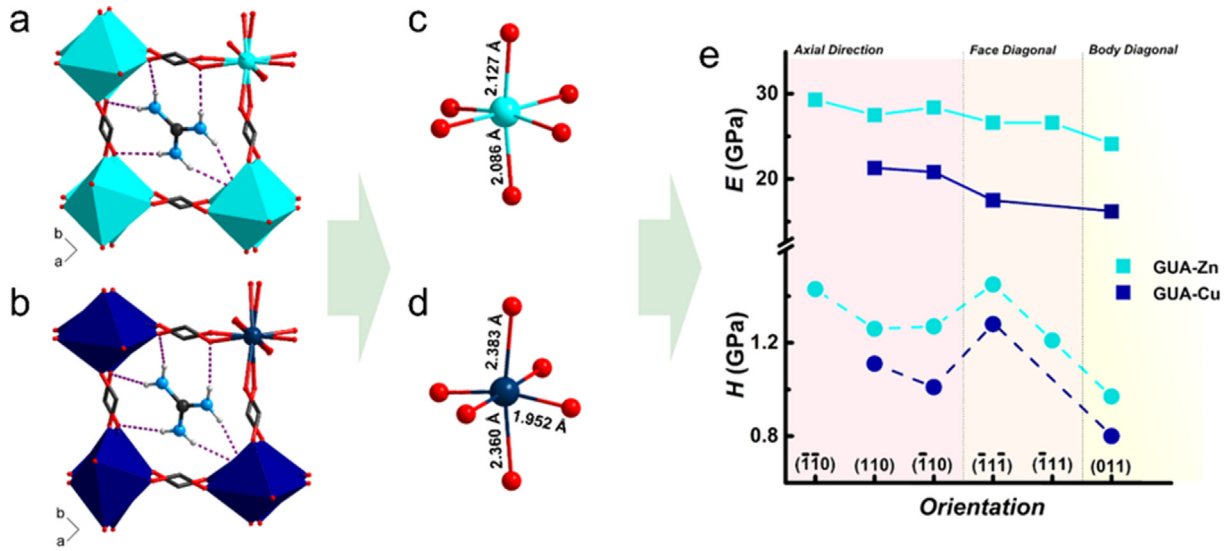

Fig. 3. Structural diagram of (a) (GUA)[Zn(HCOO)$_3$] (GUA-Zn) and (b) (GUA)[Cu(HCOO)$_3$] (GUA-Cu) viewed along (0 0 1) directions. Coordination environments of (c) Zn^{2+} and (d) Cu^{2+} ions in GUA-Zn and GUA-Cu. (e) The elastic modulus (*E*) and hardness (*H*) values of GUA-Zn and GUA-Cu are measured along the axial, face-diagonal, and body-diagonal directions of their corresponding pseudo cubic unit cell, the error bars are small and covered by the experimental data marks. Color scheme: Zn, turquoise; Cu, dark teal; N, azure; C, black; O, red; H, light gray. N–H···O bonds are shown as dashed lines. This figure is adapted with permission from Ref. [42], American Chemical Society.

bonds are compressed to 1.852–2.000 Å (Fig. 3d). Interestingly, the adjacent JT axes in GUA-Cu (Fig. 3b) within *ab* plane, arranged alternatively along [1 1 0] and [1̄10], giving rise to an anisotropic packing manner with respect to that in GUA-Zn.

Nanoindentation experiments were performed to probe the fundamental elastic and plastic properties of GUA-Zn and GUA-Cu single crystals. The values of elastic modulus (*E*) and hardness (*H*) are plotted in Fig. 3e. The moduli of GUA-Zn are strikingly 38.0%, 52.0%, and 49.0% higher than those of GUA-Cu along the axial, face-diagonal, and body-diagonal directions, respectively. As the small difference (less than 1.0%) between O-Zn-O and O-Cu-O angles does not give rise to any evident influences in framework robustness, the significant difference in mechanical strengths between GUA-Zn and GUA-Cu primarily arises from the 10.0% elongation of Cu–O bond length due to JT distortions, GUA-Cu is thus softer than GUA-Zn. Notably, when contrasting the modulus along individual directions, the smallest difference between GUA-Zn and GUA-Cu emerges in the axial direction, while their face- and body-diagonal directions exhibit larger modulus differences. As demonstrated in Fig. 3b, when indenting the pseudocubic unit cell of GUA-Cu axially and diagonally, half and all JT axis are deformed, respectively. The former indentation involves less submissive CuO_6 octahedra than the latter, therefore leading to fewer rigidity contrasts along axial directions than diagonal orientations. Indeed, regarding the hardness, the weaker resistance of GUA-Cu to plastic deformation also arises from the remarkable elongation of the Cu–O bonds along JT direction, which are more sensitive to external load and result in more ruptures, dislocations, and slippages, further leading to much lower *H* values compared with its GUA-Zn counterpart.

2.2.2. Ligand field stabilization energy (LFSE)

Tan and co-workers reported the elastic moduli of four isomorphous formate perovskites (DMA)[M(HCOO)$_3$] (DMA = dimethyl ammonium), where M = Mn, Co, Ni or Zn (Fig. 4b) [43]. The results of nanoindentation experiment on single crystals show that the moduli values increase in the sequence of Mn/Zn < Co < Ni, indicating that a small increase in radius (about 1%) between the Co^{2+} and the Zn^{2+} corresponds to the significant difference (about 16%) in elastic modulus. Moreover, the Zn^{2+} differs distinctly from Mn^{2+}

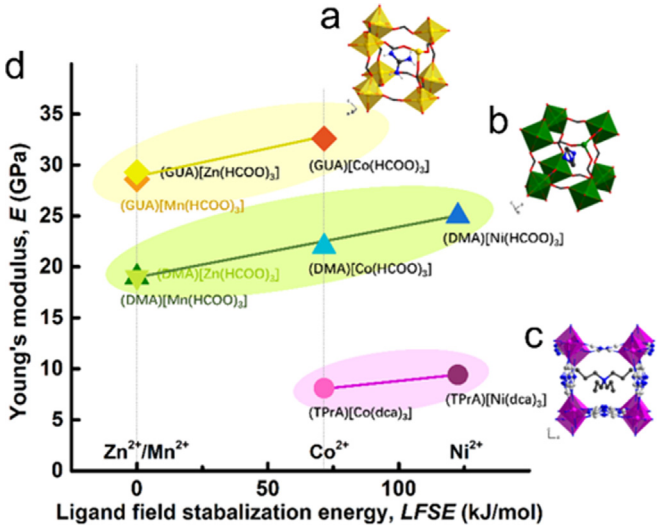

Fig. 4. Young's modulus of (a) (GUA)[M(HCOO)$_3$] (M = Co, Ni or Zn (Ref. [42])), colored in yellow), (b) (DMA)[M(HCOO)$_3$] (M = Mn, Co, Ni or Zn, colored in olive), and (c) (TPrA)[M(DCA)$_3$] (M = Co or Ni, colored in magenta) as functions of LFSEs and are fitted by linear correlations, respectively. H atoms for (b) DMA and (c) TPrA based perovskites and H bonds for all structures are omitted for clarity. This figure is adapted with permission from Ref. [43], Royal Society of Chemistry.

in size (about 9%) while their moduli along (0 1 2) orientation are almost identical (about 19 GPa). Tan and co-workers found that the LFSE of these divalent metal cations can reasonably explain the moduli variation among these HOIPs. The LFSEs of Mn^{2+} ($3d^5$) and Zn^{2+} ($3d^{10}$) are both zero arising from the half or full filled 3d electron configurations, while those of Co^{2+} ($3d^7$) and Ni^{2+} ($3d^8$), by contrast, are 71.5 and 122.6 kJ mol^{-1}, respectively (Fig. 4d). The elastic deformation of the (DMA)[M(HCOO)$_3$] perovskites has been reported as a result combing the distortions of the formate linker, the MO_6 octahedra distortion, and the M-O-C bridging angle. For the four isostructural HOIPs, these contributed factors are checked to be identical except for the MO_6 octahedra distortion. The large LFSE values of the Ni^{2+} and the Co^{2+} lead to the higher resistance against the MO_6 octahedra distortion, leading

to the stiffer mechanical feature of the perovskite framework, and vise versa.

Another study on the impact of LFSE on mechanical impact was conducted in the $(GUA)[M(HCOO)_3]$ (GUA = guanidinium) family by Feng and co-workers [44], where Co^{2+} or Mn^{2+} cation occupied the metal center and form the analogous framework structures with organic ions (Fig. 4a). The nanoindentation measurements were performed on the natural {0 1 0} facet for both the two HOIPs. The $(GUA)[Co(HCOO)_3]$ framework is about 12% stiffer than its Mn counterparts (Fig. 4d) as expected. Moreover, in order to demonstrate that the LFSE theory can be used to outline the mechanical nature of isostructural HOIP families based on various metal centers, the stiffness of the $(TPrA)[M(DCA)_3]$ analogue perovskites (TPrA = tetrapropylammonium, M = Co or Ni, DCA = dicyanamide) (Fig. 4c) also have been probed as supplementary [36]. The elastic modulus value of $(\bar{1}10)$ plane of $(TPrA)[Co(DCA)_3]$ is about 16% larger than it of $(TPrA)[Ni(DCA)_3]$ (Fig. 4d).

2.3. Linker (X-site) effects: bonding strength and flexibility

2.3.1. Electronegativity and B–X bond strength

Considering the mechanical properties of hybrid halide perovskites, the electronegativity of the bridging halogen atoms and metal-halide bond strength play a major role in framework stiffness. This has been extensively studied in halide HOIPs. Sun et al. [21] report the elastic and plastic behaviors of $MAPbX_3$ (MA = methylamine, X = Cl, Br or I) single crystals (Fig. 5a–c). The experimental Young's moduli present a general trend of $E_{Cl} > E_{Br} > E_I$, which is consistent with the trend of theoretical bulk modulus calculated by Giorgi et al [45]. From Cl to Br to I, the electronegativity of the halogen decreases, resulting in a reduction in Pb–X bond strengths and the decreasing Young's moduli (Fig. 5d). Surprisingly, the hardness varies in an opposite trend, $H_{Cl} < H_{Br} < H_I$, probably due to the reduction of structural symmetry (Cl > Br > I), which generates more dislocation systems under the external indentation pressure. In addition to this, Cahen et al. [22] also quantified the mechanical properties of $APbX_3$ (A = Cs, MA, X = I and Br) via nanoindentation and obtained the same conclusion. Moreover, Feng [18] provided theoretical insight of $MABX_3$ (B = Sn and Pb, X = Cl, Br and I) by density functional theory (DFT), the mechanical metrics extracted from elastic constants agree well with the above experimental results.

Several years later, Sun and co-workers reported the mechanical properties of the $FAPbX_3$ analogue (FA = formamidinium, X = Br or I) [19], where both the FA based bromine lead HOIP and iodine lead HOIP crystallized in cubic system. The effect induced by electronegativity of X-site linker has been observed here as well, which prolongs the Pb–X bonds and weakens the elastic modulus and hardness of $FAPbBr_3$ in contrast to its I-based counterpart (Fig. 6a). More importantly, it was found that the replacement of MA cation by larger FA cation can unexpectedly weaken the rigidity of its inorganic framework along all indentation directions, which results from the small increase in the length of Pb-Br bond by about 1%. Furthermore, the high tolerance factor of $FAPbBr_3$ (about 1.01) indicates that this structure has reached the threshold of maintaining stability for 3D perovskites. The approximately 41% lower phase transition pressure of $FAPbBr_3$ with respect to

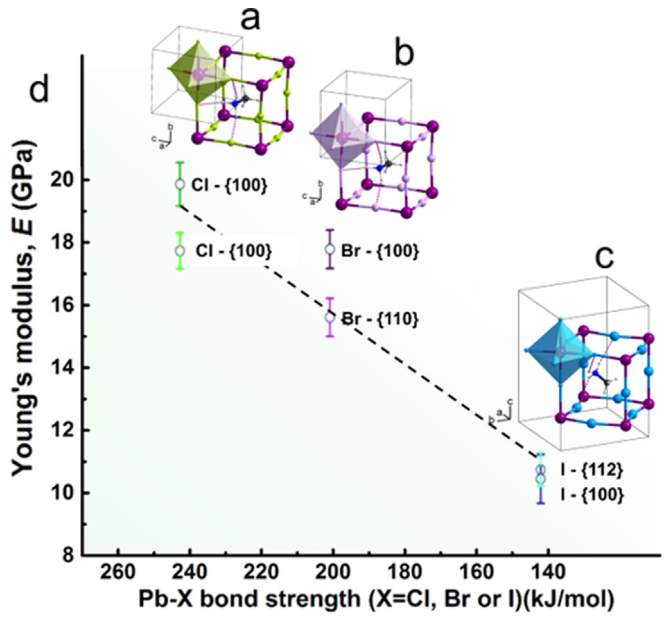

Fig. 5. Structural diagrams of (a) cubic $MAPbCl_3$, (b) cubic $MAPbBr_3$, and (c) tetragonal $MAPbI_3$. Color scheme: Pb, violet; Cl, lime; Br, lavender; I, light blue; C, dark; N, azure; H, light gray. (d) Young's moduli along orientations of $MAPbX_3$ as a function of bond strength (Ref. [46]). The dotted line gives a guide to the eye. This figure is adapted with permission from Ref. [21], Royal Society of Chemistry.

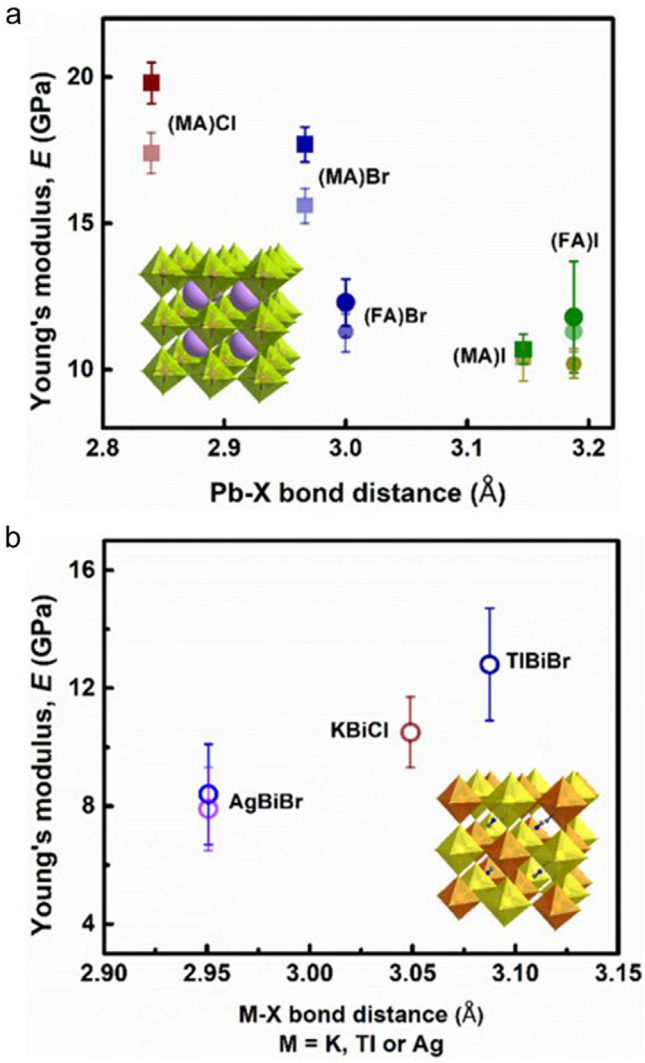

Fig. 6. Young's modulus (E) of (a) single MA and FA based halide perovskites as functions of Pb-halogen bond distance, the inset indicates the typical crystal structure of MA/FA halide HOIPs. *E Vs M-halogen bond distance* of double hybrid MA_2MBiX_6 (M = K, Tl or Ag, X = Cl or Br) are plotted in (b), the inset indicated the typical crystal structure of double MA-based halide perovskites. This figure is adapted with permission from Ref. [19], Wiley-VCH.

$MAPbBr_3$ further verifies the larger mechanically flexibility of the former [19].

In addition to the single ABX_3 hybrid perovskite, Sun and co-workers also summarized the reported mechanical properties of double perovskites with a formula of A_2MBiX_6 [19,47], in which the A and M are MA^+ and monovalent K/Tl/Ag cation, respectively. The K, Tl or Ag metal cations alternatively locate on the B-site with trivalent Bi cation, and the Br or I halogen atom locate on the X-site. Compared with $MA/FAPbX_3$ families, the replace of B-site Pb cation with monovalent and Bi^{3+} metal cation lower the overall framework stiffness of double perovskites (Fig. 6b). This trend possibly results from the weaker bonding between the monovalent ion and the halide, leading to an elastic deformation at relatively low stress. Moreover, the nonlinear plots are shown in Fig. 6b suggests that the presence of mono- and tri-valent metal cations in MA_2MBiX_6 perovskites deranges the uniformity of the bonding mode and the elastic response of the double perovskites, which cannot be represented by a single-bond distance.

Further work by Reyes-Martinez et al. [48] gave an insight into the rate-dependent mechanical behavior in the bulk $MAPbX_3$ (X = Br and I) single crystals, especially the creep and stress relaxation behavior. These results show that the viscoplastic behavior may arise mainly from the soft anionic perovskite frameworks. As the plastic deformation can nucleate dislocations when it occurs in the single crystals during nanoindentation, the strain hardening may responsible for the reduction in the rate of penetration for all tested materials. The creep displacement of $MAPbBr_3$ is much larger than that of $MAPbI_3$, indicating the former possesses more slipping systems than the later (Fig. 7a). Moreover, the discrete magnitudes of relaxation for $MAPbBr_3$ and $CsPbBr_3$ (Fig. 7b) indicate that the stiffness of Pb–X framework is a dominant factor influencing the dynamic mechanical response of these hybrid perovskite single crystals.

2.3.2. Linker configuration and flexibility

The flexibility of HOIPs frameworks is not only affected by metal-linker bonding strength but also the chemistry ingredient and geometry shape of the linkers which furthering constitute the configuration. In this part, we review how the distortion of M-X-M bonding mode, such as bending and twisting, tunes the macro performance of perovskites under the external load.

Wu et al. [49] reported a new family of hybrid perovskites (Am)$[Mn(H_2PO_2)_3]$ (Am = GUA, FA, imidazolium), where the hypophosphite ligand is chemically and structurally similar with formate ligands (Fig. 8). (Am)$[Mn(H_2PO_2)_3]$ show significantly greater cage distortions in contrast with their formate counterparts, leading to additional symmetry-breaking elements in the form of classically forbidden Glazer tilts and columnar shifts [50]. We here exemplify this transformation through the monoclinic (GUA)$[Mn(H_2PO_2)_3]$, in which the GUA^+ cations off-centring occupy the $[Mn(H_2PO_2)_3]^-$ cage and lie parallel to one plane (Fig. 9a). Since we can not directly compare this hypophosphite perovskite (GUA)$[Mn(H_2PO_2)_3]$ due to their different crystal system, Wu et al. definite a "distortion factor", δ (Eq. (1)), to index the structural deviation from the cubic aristotype.

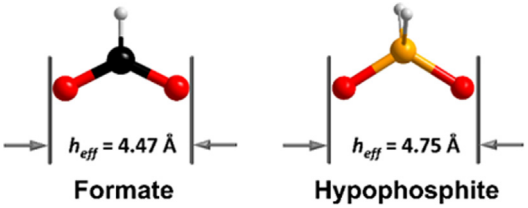

Fig. 8. Structures of a formate and a hypophosphite molecule. Color scheme: C, black; O, red; H, light gray; P, orange. This figure is adapted with permission from Ref. [49], American Chemical Society.

$$\delta = \frac{V_{ideal}}{V_{real}} - 1 \quad (1)$$

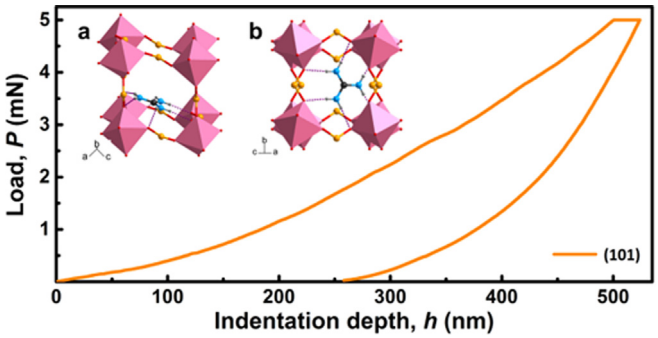

Fig. 9. Typical nanoindentation *P-h* curve normal to the (1 0 1) face of a single crystal of (GUA)$[Mn(H_2PO_2)_3]$ (Ref. [36]) measured via a Berkovich indenter. Inset: structure diagrams of (GUA)$[Mn(H_2PO_2)_3]$ viewed along different orientations. Color scheme: Mn, pink; P, light orange; O, red; C, black; N, azure. N–H···O bonds are shown as purple dash lines. The H atoms of hypophosphite ligand are omitted for clarity.

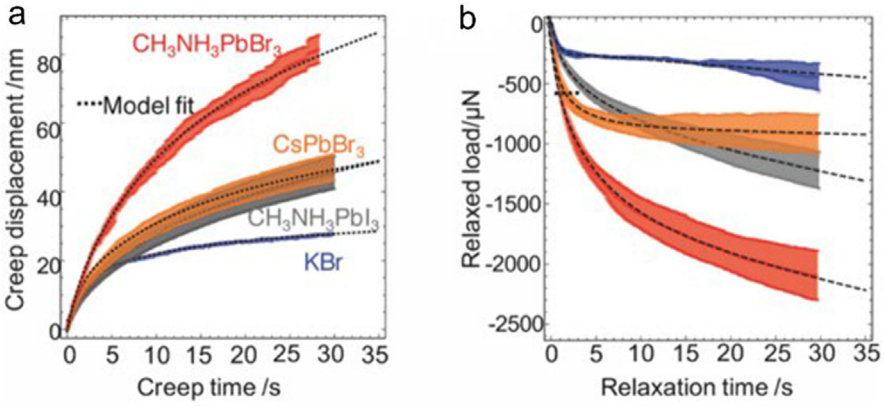

Fig. 7. Typical (a) creep displacement curves and (b) load relaxation curves for $MAPbX_3$ (X = Br and I), $CsPbBr_3$ and KBr. This figure is adapted with permission from Ref. [48], Wiley-VCH.

V_{idal} is the volume of an idealized cubic cage that the length of the sides equal to the average crystallographic M-M distance, and V_{real} is the actual volume of a single $[Mn(H_2PO_2)_3]^-$ cage. The δ of hypophosphite perovskite is about 20% larger than it of formate perovskite, revealing the H_2POO^- is easier to be flexed under indentation. It may explain the weak stiffness of hypophosphite perovskites with Young's modulus and hardness of about 16.57 GPa and 1.20 GPa (Fig. 9) [36], respectively, when loading external stress normal to the plane of GUA^+ cations (Fig. 9b). The same rule applies to FA and imidazolium hybrid perovskites, for which the adoption of formate or hypophosphite on X-site makes a significant difference.

The mechanical behavior of a highly distorted azido-bridge perovskite (DMA)$[Mn(N_3)_3]$ also has been investigated by performing the nanoindentation normal to its two naturally grown facets of single crystals [36]. The average values of Young's moduli (E) and hardness (H) extracted from the P-h curves (Fig. 10d) are 10.38 and 0.53 GPa for (1 0 0) face (Fig. 10a), and 11.78 and 0.39 GPa for (0 0 1) plane (Fig. 10b), respectively. In this case, the azido ligands serve as holders and form a stiffer morphology between the (0 0 1) faces than between the (0 0 1) planes. The underlying crystal structure was examined by measuring the deviation between the azido ligands atoms and the load direction. For example, as shown in Fig. 10c, the ligand along c-axis is formed by nitrogen atoms N1, N2 and N3 which depart from (0 0 1) orientation by 6.7°, 9.7° and 18.6°, respectively. While the N4, N5, and N6 deviate from (1 0 0) direction with larger magnitudes of 4.1°, 12.7° and 20.7°, respectively, leading to a softer resistance of deformation and smaller elastic modulus along (1 0 0) orientation. As the plastic deformation in non-twinned molecular crystals occurs via slip [41], the substantial contrast between the hardness of (1 0 0) and (0 0 1) plane can be ascribed to the disparity in their hydrogen-bonding modes (Fig. 10a-b).

The effect of M-X-M bending on the framework rigidity is also observed in the prototypical MA lead halide perovskite [19], in which the unit cell of tetragonal $MAPbI_3$ is smaller than that of cubic $FAPbI_3$, while the Pb–I bond lengths are similar for both structures. The Pb–I–Pb bond angles of $MAPbI_3$ are found to be deflected from 180° due to the PbI_6 octahedral tilting, which is liable for the easy occurrence of its elastic deformation along ⟨1 0 0⟩. In addition, the bending of angles also reveals the fact that this tetragonal structure is more densely packed than its tolerance factor predicts.

3. Behaviors of halide perovskites under pressures

The reported high-pressure studies of HOIPs to date mainly focus on hybrid halide perovskites, and few works refer to other classes of hybrid perovskites [51]. In general, halide perovskites undergo phase transition under hydrostatic pressure of ~0.2 GPa. In their review article, Lu et al. have summarized the recent advances of behaviors of halide perovskites under high pressure [52], which includes the pressure-stimulated structural evolutions and associated property changes [31,53–65]. Therefore, the authors do not repeat the summary here.

4. Abnormal mechanical properties and the barocaloric effect

4.1. Abnormal mechanical properties

Unconventional mechanical properties of materials, such as negative Poisson's ratio (NPR), negative linear compressibility (NLC), and negative thermal expansion (NTE), remain the active areas of research and have made significant progress in the past decade on understanding the exotic nature of physics and detecting the performance [66–68]. Materials with NPR expand in the perpendicular direction when they are stretched. This macroscopic behavior is connected to a material's properties on the microscale. For example, the auxetic metal electrodes can improve the sensitivity of NPR/piezoelectric composites by enlarging the effect of an applied in-plane uniaxial strain on the sensor sheet area [69]. Moreover, NPR can also enhance the materials' toughness to resist fracture [70]. Taking this perspective, the NPR materials have potential applications in pressure detector, robust shock absorbing materials, and body armor [71]. Notwithstanding the NPR effect does not violate thermodynamics, it is rare in crystalline solids [72]. The pioneering investigation is typified by foams with reentrant honeycomb [73], zeolites [74], and cubic lattice metallic alloys [69,75]. Dong and co-workers firstly took stock of NPR in $BaTiO_3$ ceramic near the Curie point in ferroelastic transition [76]. Huang et al. further demonstrated that these analogous perovskite oxides possess anisotropic PR (Poisson's ratio) range from negative to large positive values beyond isotropic upper limit [66,77]. However, no direct observation of NPR in HOIPs or theoretical predictions on their NPR were reported to date. Another hitherto undetected mechanical behavior in HOIPs is NLC, referring to a material that expands along a specific direction when it is exposed

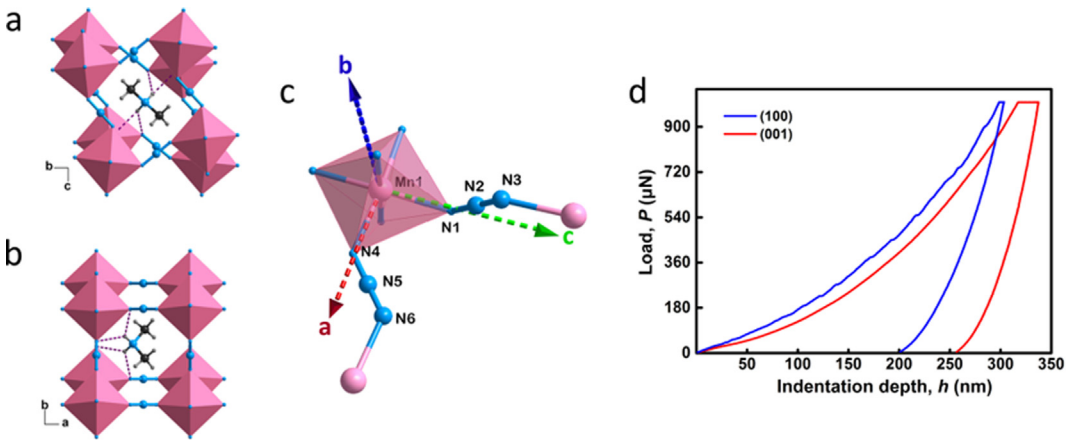

Fig. 10. Structural diagrams of orthorhombic (DMA)$[Mn(N_3)_3]$ viewed along (a) (1 0 0) and (b) (0 0 1) orientations, the purple dash lines represent the N–H···O bonds. Color scheme: Mn, pink; C, black; N, azure; H, dark gray. (c) Asymmetric unit and its principal axis are presented to quantify the deviation of the azido ligand from indentation direction. (d) Load-indentation depth (P-h) curves of indentation normal to the (1 0 0) and (0 0 1) planes of (DMA)$[Mn(N_3)_3]$ single crystal (Ref. [36]).

to hydrostatic pressure and undergoes an anisotropic shrinkage [78]. Similarly, as an accurate macro reaction lies on mechanical stimulus, NLC also comes into play in many interesting research areas, for instance, tailoring the coupling performance of NLC and other properties by tuning this abnormal pressure dependency. By comparison, NTE describing material's compression behavior upon heating is relatively common in HOIPs. The HOIPs with NTE effect have been systematically discussed on account of the relationship between framework flexibility and chemical compositions by Goodwin et al, and the work critically analyzed the influences formed from metal cation size, organic amine cation size and the associated asphericity type [29]. In this section, we will review the complementary studies on NPR and NLC of HOIPs based on calculations derived from elastic constants of single crystals which provided by preceding reports [44,46] and the supplementary calculations carried by the authors of this manuscript.

4.1.1. Negative Poisson's ratio (NPR)

For mechanically anisotropic perovskites, the PR varies with stress/strain orientation and can no longer be predicted like in isotropous systems, Evans et al. carried out a solution based on tensorial operations (inversion, rotation, and diagonalization) [79]. As shown in inorganic perovskites, structures with a higher degree of anisotropy usually exhibit larger orientation-dependent extremes and easily give rise to NPR performance [66], PRs of five HOIPs were presented in Table 1, including $(MA)MX_3$ (M = Pb or Sn, X = Cl, Br or I) and the more flexible $(MA)[Mn(HCOO)_3]$ from reported elastic constant tensors [18,44] of single crystals.

The orientation dependent PRs of the five HOIPs (Table 1) are exemplified through the orthorhombic MAPbI3 (Fig. 11). Based on the symmetrically distributed PR values in 3D sphere space (Fig. 11a), the rotational angles are restricted in an asymmetry region [66]. For example, the value of α was discussed in the range from 0° to 90° (Fig. 11b), the same as β and γ (Fig. 11c-d). The value of PR plotted in Fig. 11b-d as a function of the orientation. The minimum part of PR distributes in (1 0 0) plane (Fig. 11b) with positive values at 0°, and further gets closer to zero and gradually becomes negative at α = 54°. While the minimum part of PR distributing in (0 1 0) plane (Fig. 11c) contains two discrete NPR regions, which ranges from 30° to 60° and 67° to 90°, respectively, and further reaches the minimum magnitude of −0.61 at β = 90°. Notably, the minimum part of PR continuously stays negative in the entire angle range (Fig. 11d) and reaches the minimum magnitude of −0.64 at γ = 18.5°. Interestingly, such NPR is not found in other phase halide perovskites, such as tetragonal or cubic $MAPbI_3$, which does not conform to the previous report that the NPR performance can be detected in 69% cubic metals. In addition, it was found that the gaps between the two extreme positive values of PR for these HOIPs are narrowed as the symmetry rises. For example, the PR of tetragonal and cubic $MAPbI_3$ range from 0.07 to 0.77 and 0.23 to 0.32, respectively, the gap is lessened from 0.7 to 0.09. This is probably led by the higher crystallographic symmetry, which gives more constraints on elastic tensors and intrinsically favors isotropy [80]. Likewise, for $MAPbBr_3$, the PRs in tetragonal and cubic phase range from 0.62 to 0.16 and 0.53 to 0.10, respectively, and the gap narrows from 0.46 to 0.43.

The extremums values and corresponding orientations of the NPR for each orthorhombic halide hybrid perovskites are listed in Table 1. The universal anisotropic index (A) was introduced to analyze this diverse PR values in different perovskite systems, where G^V, G^R, K^V, and K^R are the shear and bulk moduli calculated by Voigt and Reuss approximations [81], respectively. As shown in Table 1, the values of A for the HOIPs cover a large numerical scope while the magnitudes of PRs fluctuate feebly in a relatively small range. Among these HOIPs, $MASnI_3$ with largest anisotropy 28.59 shows the minimal NPR value along [0 2 −1] and maximum auxetic behavior along [1 0 2], $MAPbBr_3$ with most moderate anisotropy exhibits a largest NPR value and a minimum PR range. The range of PR value of $(MA)[Mn(HCOO)_3]$ is unexpectedly smaller than that of $MAPbI_3$ while the anisotropic index of the former is larger than the latter, it is probably due to the flexibility of formate linker.

Rigid mechanical model, rotating hinged rectangles, is established based on the $MAPbI_3$ structure projected along b-axis (Fig. 12a) to typically replicate auxetic behavior for halide perovskite analogue. The azure rigid rectangles (Fig. 12b) correspond to the 2D projections of PbI_6 octahedron which are linked by Pb–I–Pb hinges to form a columnar structure arranged parallel to (0 1 0) direction. Therefore, the rotation of rectangles will result

Table 1
The minimum and maximum values of Poisson's ratio, the extreme values' orientation, and the anisotropic indexes of HOIPs by calculations.

HOIPs	Phase	ν_{min}	ν_{min} Dir.	ν_{max}	ν_{max} Dir.	A [81]
$MAPbI_3$ [18,36]	Ortho.	−0.64	[3 1 0]	1.36	[1 0 1]	5.19
$MAPbBr_3$ [18,36]		−0.12	[0 1 1]	0.69	[2 3 $\bar{4}$]	1.13
$MASnI_3$ [18,36]		−1.60	[0 2 $\bar{1}$]	2.13	[1 1 0]	28.59
$MASnBr_3$ [18,36]		−0.29	[0 1 0]	0.88	[1 0 0]	1.65
$[MA][Mn(HCOO)_3]$ [36,44]		−0.19	[3 1 3]	0.89	[1 1 1]	5.42

Ref. [81] $A = \frac{5G^V}{G^R} + \frac{K^V}{K^R} - 6.0$.

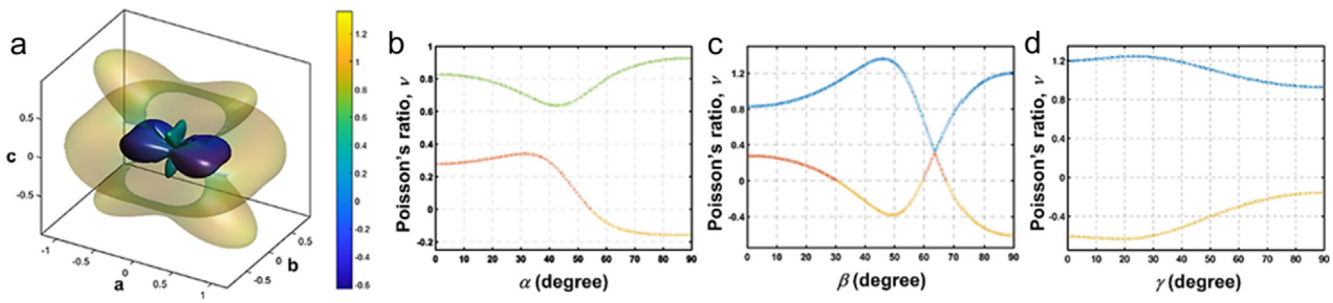

Fig. 11. Poisson's ratio (PR) of orthorhombic $MAPbI_3$. (a) 3D distribution of PR values is scaled by radian in the spherical coordinate system, the maximum part and minimum part of PR values in sphere space symmetrically forming the transparent and the opaque surfaces, respectively. 2D plots in rectangular coordinates system of PR (ν) projected normal to (b) (1 0 0) plane, (c) (0 1 0) plane, (d) (0 0 1) plane. α, β and γ (0–90°) are the orientations of PRs deviated from a-, b- and c-axis in (1 0 0), (0 1 0) and (0 0 1) planes, respectively. Color scheme: maximum part of PRs, green and blue; minimum part of PRs, orange, and red.

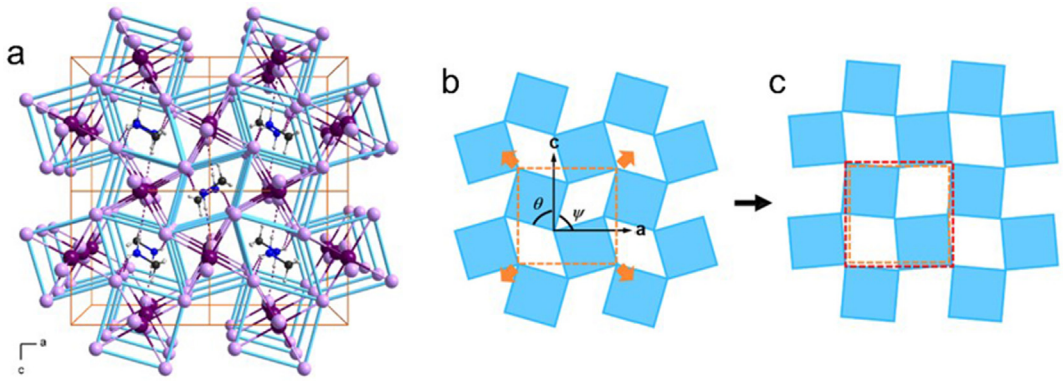

Fig. 12. The schematic illustration for achieving negative Poisson's ratio in orthorhombic $MAPbI_3$. (a) The geometric features in $MAPbI_3$ viewed along [0 1 0] direction, iodine atoms and the azure linkages between adjacent iodine atoms forming the 'hinges' and the 'rectangles', respectively. (b, c) An idealized model shows the molecular level behavior for performing NPR, the azure 'rectangles' is the simplified 2D mode of PbI_6 octahedron projected norm to (0 0 1) plane, the 'rectangles' is assumed to be non-deformed upon loading. θ and ψ are the angles between the 'rectangles' edges and the principal axes. The area marked by the yellow frame is expanded as the red frame marked area after auxetic behavior. Color scheme: Pb, violet; I, lavender; C, black; N, blue; H, light gray. H bonds are represented by purple dash lines.

in Pb–I–Pb deformation when loaded [82,83]. Considering the 'rectangles' are quadrilaterals in the original structure, the angles, θ and ψ, are introduced to quantify the rotation in synergy [84]. When loading stress along directions in the (0 1 0) plane off-axially, both θ and ψ increase gradually to 90° (Fig. 12b) to achieve auxetic performance (Fig. 12c). Moreover, the load along *a*-axis gives rises to the NPR in (1 0 0) plane (Fig. 11b) and reaches maximum auxeticity at $\alpha = 90°$ (along *c*-axis). When loading along *c*-axis, the auxetic behavior occurs on the (0 0 1) plane (Fig. 11d) and with a magnitude of −0.61 at $\gamma = 0°$ (along *a*-axis). For different HOIPs, the initial angle between the rectangles varies. All the NPR values in this manuscript are extracted from elastic constants tensors calculated by the first-principles calculation.

4.1.2. Negative linear compressibility (NLC)

The above HOIPs are also found to have anisotropic NLC in their orthorhombic phase based on the same elastic stiffness tensor matrixes used in NPR calculations [18,44]. However, the high hydrostatic pressure XRD experiments have not detected any diffraction peak shift to the low diffraction angle, namely axially or off-axially expansion. The lack of the experimental evidence of NLC in hybrid perovskite may arise from three main factors: the structure of materials, the resolution of diffraction light source and the range of hydrostatic pressure applied in the experiments.

4.2. The barocaloric effects

The barocaloric effect is known as the isothermal entropy change or adiabatic temperature change in response to the application or withdrawal of external pressure. The term is originally used in gas cooling technologies. The barocaloric effect in solid-state refrigeration [85] is first observed in a polycrystalline ceramic $Pr_{1-x}La_xNiO_3$, where the application of hydrostatic pressures up to 0.5 GPa led to a small effective cooling with comparable elastic heating losses [86,87]. Recent efforts, therefore, have been focused on searching for materials showing large caloric effects close to room temperature when stimulated by a moderate pressure. For example, the magnetic alloy Ni-Mn-In was found to show a large barocaloric effect of 24.4 J kg^{-1} K^{-1} under a pressure of 0.26 GPa that is comparable to the giant magnetocaloric effect of this material [88]. Considering the caloric effects usually occur at the first-order phase transition of materials [89], hybrid perovskites with structural phase transition nature furthering attract attention for their solid-state cooling potential expanding their possibility for new applications.

Recently, (TPrA)[$Mn(dca)_3$] was reported to exhibit big isothermal entropy change of 37.0 J kg^{-1} K^{-1}, driven by relatively small hydrostatic pressure less than 0.007 GPa slightly above room temperature [14]. (TPrA)[$Mn(dca)_3$] shows first-order phase transition at around 330 K (T_c), during which the TPrA-2 ($T > T_c$) possesses much more disorders than TPrA-1 ($T < T_c$) (Fig. 13) [90]. Based on these two structures, the configurational entropy (ΔS_{config}) can be calculated as $R\ \mathrm{In}(n_1/n_2)$, where n_1 and n_2 are numbers of configurations in the two HOIPs and R is the gas constant [91]. In this report, the DSC (differential scanning calorimetry) are performed as a function of pressure, the measured large entropy change (ΔS_{trains}) of about 42.5 J kg^{-1} K^{-1} at ambient pressure agrees well with the value of calculated ΔS_{config}, suggesting the configurational factor dominate the total entropy change in this hybrid perovskite. Moreover, under pressures from 1 to 1000 bar (that is 0.0001–

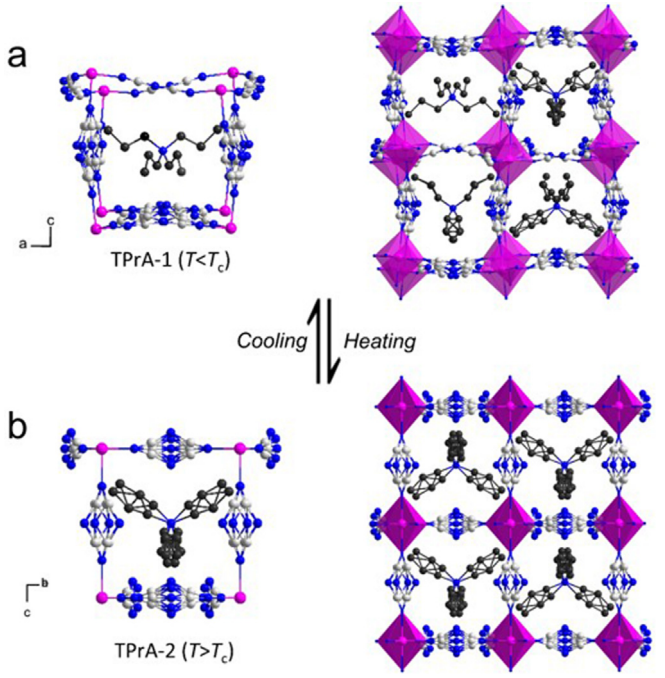

Fig. 13. Structure diagram of (TPrA)[$Mn(dca)_3$] in (a) low-temperature phase (TPrA-1) and (b) high-temperature phase (TPrA-2). Color scheme: Mn, magenta; C, light gray and black; N, blue. The H atoms are omitted for clarity.

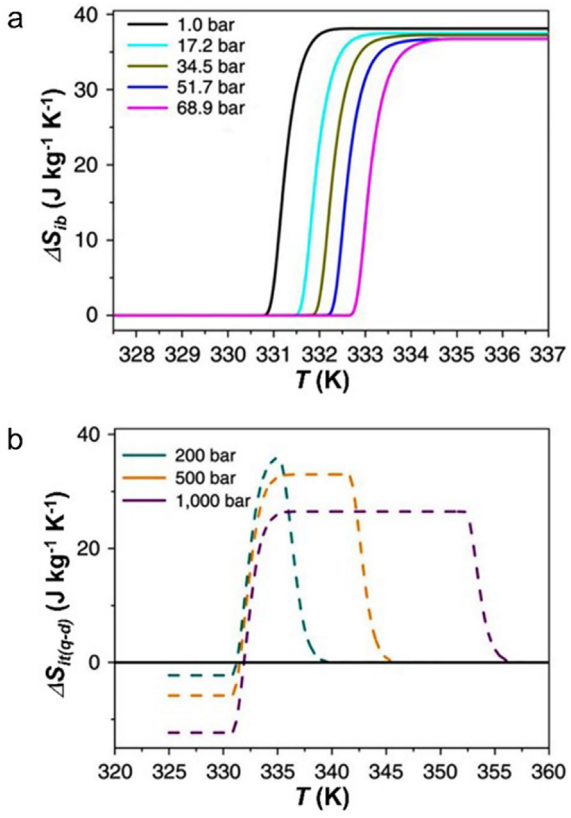

Fig. 14. The barocaloric effect of (TPrA)[Mn(dca)$_3$]. (a) Isobaric entropy changes (ΔS_{ib}) as a function of temperature in the low-pressure range (1 to 68.9 bar). (b) Barocaloric effect quantified via isothermal entropy changes ($\Delta S_{it(q-d)}$) by a quasi-direct method. Note: The $\Delta S_{it(q-d)}$ curves have been offset the depletion arising from the additional entropy change at each pressure. This figure is adapted with permission from Ref. [14], Nature Publishing Group.

0.1 GPa), the resulted phase transition temperature (T_c) gradually rises as pressure (P) increases, giving a barocaloric coefficient ($\partial T_c/\partial P$) of 231 K kba^{-1}. The almost invisible deviation between the T_c *Vs* P in heating and cooling indicates a small hysteresis of about 0.9 K.

The barocaloric effect for this material was probed in two pressure regions: low pressure (P < 70 bar) and higher pressure (up to 1000 bar). In the low-pressure region, the temperature-dependent isobaric entropy change, ΔS_{ib}, increases up to a plateau of about 38.1 J kg^{-1} K^{-1} (Fig. 14a) when the perovskite undergoes a phase transition from TPrA-1 to TPrA-2, suggesting the maximum value of entropy attainable in this structural transition. Moreover, the entropy curves progressively move toward higher temperature when pressurized. The isothermal entropy change ($\Delta S_{it(q-d)}$), calculated as the difference between the isobaric entropy change (ΔS_{ib}) at different pressures by quasi-direct method, was defined to quantify the barocaloric effect of this materials and reached a maximum value of 37.0 J kg^{-1} K^{-1} when the isothermal application of pressure up to 68.9 bar. Meanwhile, the associated adiabatic temperature change ($\Delta T_{ad(q-d)}$) was calculated as about 5.0 K. The authors also investigated the higher pressure region, where the entropy started to diminish significantly and resulted in a decrease of the barocaloric effect due to the suddenly increased losses from additional changes in isothermal entropy related to elastic heat (Fig. 14b). For example, the reduction of about 32% for ΔS_{ib} at P = 1000 bar gives rise to a $\Delta S_{it(q-d)}$ of about 26.5 J kg^{-1} K^{-1}. The challenges raised from thermal hysteresis and reversible entropy changes are also referred to in this work, we will not cover these aspects again.

Shortly after in another report, the large barocaloric effect of 39.9 J kg^{-1} K^{-1} was witnessed in the formate (DMA)[Mg(HCOO)$_3$] perovskite by applying pressure up to 0.206 GPa [92]. DMA cations in high temperature (DMA-1) was disordered in a threefold way (Fig. 15a) [93], while the DMA cations at low temperature (DMA-2) was solved and refined by taking into account the crystal twinning due to the presence of ferroelastic domains (Fig. 15b). This structural variation is compatible with the configurational entropy change of 9.13 J kg^{-1} K^{-1}, whereas the experimental transition entropy gain is somewhat higher. This discrepancy might result from the additional degrees of disorder, including the rotations of methyl CH_3 groups about the N-C bonds, the change of volume during the transition and other processes affecting the free energy of the crystal. In addition, the DMA cations' disordering engages all proton-accepting sites of the carboxylate groups in N–H···O hydrogen bonds, which dynamically formed and broken, but it averages the attracting guest-host interactions, while bonds Mg–O and the MgO_6 octahedra volume are not affected by the transition. Therefore, the temperature-dependent unit cell volume shows a stepwise drop of 0.36% at the transition point in the heating run. Moreover, this volume change indicates a negative barocaloric coefficient ($\partial T_c/\partial P$) in accordance with the Clausius-Clapeyron equation. The transition temperatures (T_c) read from DSC curves decreases for both cooling and heating runs with pressure increases (from 0.1 to 887 MPa). In the pressure range of 0.1 to 400 MPa, the $\partial T_c/\partial P$ for cooling and heating are −45.9 and −40.2 K/GPa, respectively, indicating a gradually dissipating thermal hysteresis, which finally vanishes at about 400 MPa, namely tricritical point (TCP) [94].

The pressure-induced degeneration in isobaric entropy change (ΔS_{ib}) is observed both in heating and cooling runs with increasing pressure (Fig. 16a), which can fully reverse during decompression cycles and thus might originate from the elastic heat effect. These additional entropy changes ($\Delta S_+(p)$) induced by the pressure of 887 MPa, at 245 and 290 K, are estimated to be −28.9 and −38.7 J kg^{-1} K^{-1} by Maxwell relation $m^{-1}(\partial V/\partial T)_p = -(\partial S/\partial p)_T$,

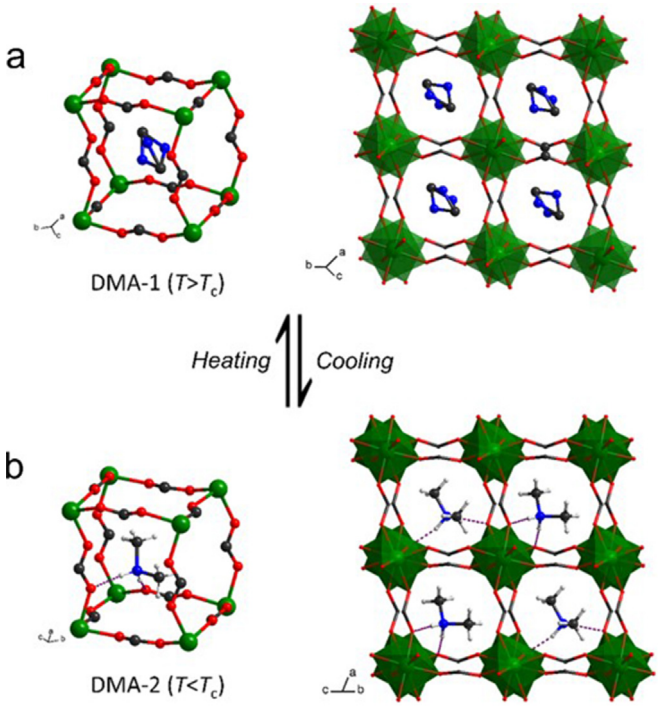

Fig. 15. Structure diagram of (DMA)Mg[HCOO]$_3$ in (a) high-temperature phase (DMA-1) and (b) low-temperature phase (DMA-2). Color scheme: Mg, olive; N, blue; C, black; H, light gray. H atoms in the formate ligands are omitted for clarity. hydrogen bonds N–H···O are indicated by the dashed lines.

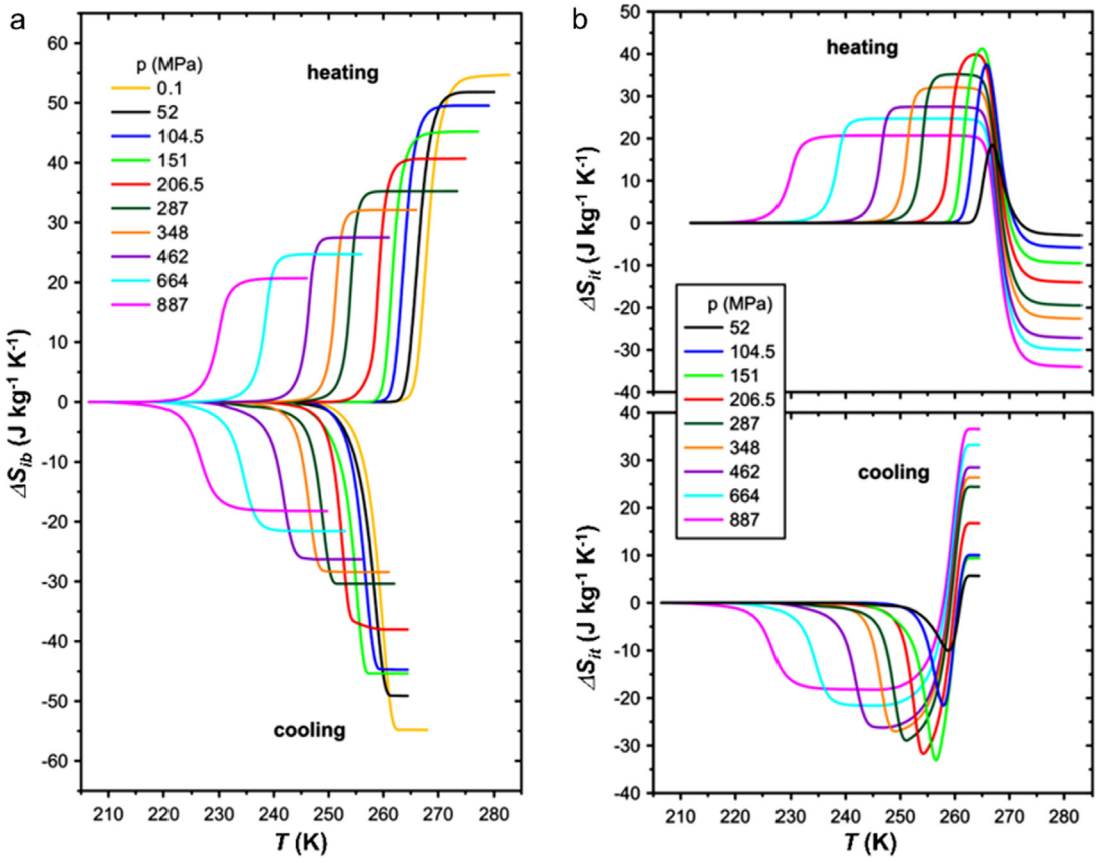

Fig. 16. Barocaloric effect in (DMA)[Mg(HCOO)$_3$]. (a) Isobaric entropy change (ΔS_{ib}) runs as a function of temperature at pressures ranging from 0.1 to 887 MPa. (b) Barocaloric effect (ΔS_{it}) at a certain pressure (P_o) is quantified as the difference between ΔS_{ib} ($P_o \neq 0.1$ MPa) and ΔS_{ib} ($P = 0.1$ MPa) curves by a quasi-direct method. This figure is adapted with permission from Ref. [92], American Institute of Physics.

respectively. Taking these aspects, the discrepancy of about 9.8 J kg^{-1} K^{-1} in elastic heat can be expected between the low- and high-temperature phases, however the experimentally observed decrease in ΔS_{ib} amounts to 34 and 36.6 J kg^{-1} K^{-1} for cooling and heating, respectively. The changing character of the transition associated with the step-wise volume reduction at the transition temperature partly contribute to the large decrease of the transition entropy magnitude. The isothermal entropy change (ΔS_{it}) derived from ΔS_{ib} (Fig. 16a) reach the maximum value of 41.2 J kg^{-1} K^{-1} at 151 MPa (Fig. 16b). For (DMA)[Mg(HCOO)$_3$] at 262 K, the ΔS_{ib} of 39.9 J kg^{-1} K^{-1} was motivated by pressure up to 206.5 MPa significantly outperforming among barocaloric materials. Furthermore, the specific heat C_p = 1291 J kg^{-1} K^{-1} in this temperature results in a large adiabatic temperature change ΔT_{ad} of 8.1 K. In these terms, the entropy change in the vicinity of TCP remains large and the dilution of thermal hysteresis can also be considered for barocaloric applications.

Very recently, a new hybrid perovskite (TPrA)[Cd(dca)$_3$] was synthesized and exhibits three distinct phase transitions induced by temperature changes. When this material transforms from non-isochoric orthorhombic to tetragonal phase at T_c (385 K), the reversible barocaloric effect (ΔS_{it} = 11.5 J kg^{-1} K^{-1}) was stimulated by a giant caloric coefficient of 382 K GPa^{-1} which is much larger than this value observed in other solid refrigeration materials [95]. For instance, the values of $\partial T_c/\partial P$ for $(NH_4)_2SO_4$ and (TPrA)[Mn(dca)$_3$] are 57 and 231 K GPa^{-1}, respectively. It reveals the outperformance of (TPrA)[Cd(dca)$_3$] in terms of pressure-induced barocaloric tunability. In addition, the volume changes by about 0.4% in the phase transition.

5. Thin-films and strain engineering

Owing to their promising optoelectronic properties, hybrid perovskites have been fabricated into thin-films and applied as light-harvesting layers in photovoltaic devices [12]. These perovskite absorber films are fabricated into two forms: the large-area polycrystalline films scarred by numbers of grain-boundaries, and the independently distributed single-unit-cells with some structural defects. Both the intrinsic boundaries and defects limit the stability of encapsulated devices significantly, and various preparation methods have been developed to mitigate this problem [96]. Due to the compliant nature of HOIP thin film, the internal lattice strain or external stress-strain disturbances can induce phase transitions [97–99], reduced crystallinity and defects formation [100], and hence lead to undesired consequences in the electronic properties of devices [101–105].

The initiation and propagation of cracks or defects were identified as a major trigger of material's failure. Yu et al. studied the fracture mechanical behavior and microstructural evolution of the defective $CH_3NH_3PbI_3$ thin films by large-scale molecular dynamics simulations [106]. The polycrystalline $CH_3NH_3PbI_3$ films possess only 34–53% elastic modulus of that from pristine single crystals and undergo continuous amorphization during tensile loading (Fig. 17). On the other hand, the inverse Hall-Petch relation was detected in these films, where the yield stress decreases with the grain size increasing. Further simulation work suggests that plastic deformation originates from the transformation of partial edge dislocations to nanovoids, and comparing to pristine samples, polycrystalline $CH_3NH_3PbI_3$ films with low Poisson's ratio has more

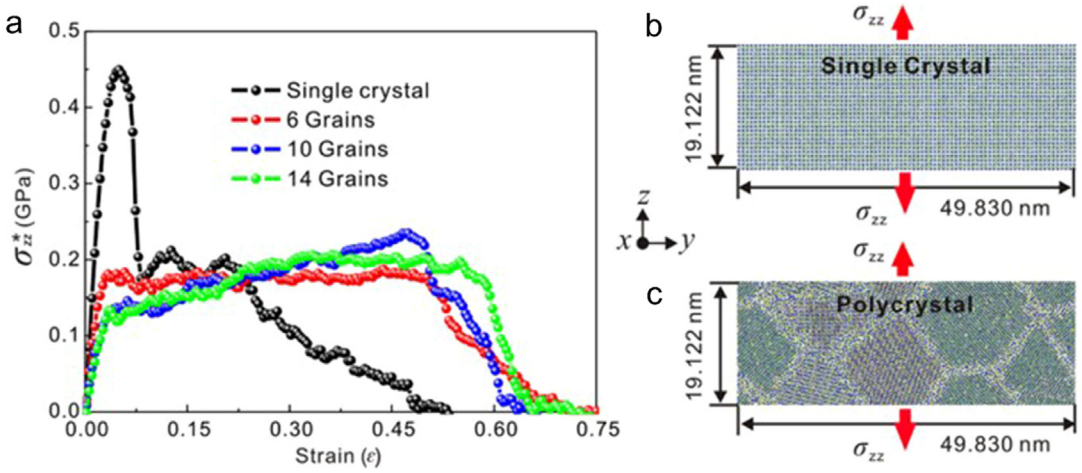

Fig. 17. (a) Calculated stress-strain curves of the cubic single and polycrystalline $MAPbI_3$ (consisting of 6, 10 and 14 grains) under tensile loading. The simulated structure of (b) mono-crystal and (c) poly-crystal. σ^{zz} and ε are the effective tensile stress and the engineering strain, respectively. Both σ^{zz} and ε are along the *z*-axis. This figure is adapted with permission from Ref. [106], American Chemical Society.

merits in strain energy absorption. Apart from the inherent defects and amorphization, the stress-strain states such as residual or thermal stresses, bending, and in-plane compression or tension also affect the stability of solar cells. Lattice strain caused by the uncoordinated thermal expansions between the $CH_3NH_3PbI_3$ layer and the substrate surface leads to lower ion migration energy and accelerate the material's degradation [101]. Furthermore, the anisotropic thermal expansion in the annealing process can induce bi-axial tensile stress in each grain of polycrystalline $CH_3NH_3PbI_3$ films [103]. Bush et al. found that the in-plane isotropic compressive stress of HOIPs in perovskite alloys such as $Cs_xFA_{1-x}Pb(Br_yI_{1-y})_3$ family could result in film wrinkling and reduce the light harvesting efficiency [107]. Taking these perspectives into consideration, methods to relax the lattice strain of HOIP architectures are desired. For instance, CH_3NH_3Br alloying has shown to cause lattice contraction, thereby balancing the lattice strain [108].

Considering the effect of stress-strain states in flexible devices, Park et al. measured the elastic modulus of the mixed halide perovskite layer $CH_3NH_3PbI_{3-x}Cl_x$ (~13.5 GPa) by multicycle nanoindentation tests, the additional simulation results of the finite element analysis indicated that the device could sustain a bending radius of 1 mm, while the power conversion efficiency of the device dropped at the bending radius of 0.5 mm [105]. This bending behavior of HOIP solar cells has been shown to contribute to the solar cell current-voltage characteristics, for which the out-of-plane current of $CH_3NH_3PbI_3$ was increased by 196% at 1 V with an application of compressive strain (0.088%) while decreased by 49% with an application of tensile strain (0.088%) [102] Spina et al. revealed the elastic modulus and hardness of $CH_3NH_3PbI_3$ can degraded up to five-fold when exposed to moisture [109].

2D non-van der Waals-type $CH_3NH_3PbI_3$ with mono single unit cell thickness were also successfully prepared [110] and their mechanical properties need to be explored. Their emergence suggests the possibility of realizing the 2D monolayer architecture for many ABX_3-type HOIPs, which possess better photovoltaic performance and a broader range of applications. The mechanical properties of these new arisen 2D ultrathin non-van der Waals-type HOIPs are still less well understood, and only few nanoindentation studies were conducted to access the out-of-plane mechanical metrics of 2D non van der Waals-type HOIPs (A_2BX_4 and $A_2A'_{n-1}B_nX_{3n+1}$) [111]. Further mechanical studies are strongly required to complement the little knowledge of these striking monolayer perovskite halides, particularly in addressing their flexibility desirable for a variety of optoelectronic applications.

Apart from halide perovskites, several studies also investigated the role of stress-strain states in formate perovskites. As shown in Fig. 18a, the Cr atoms in (GUA)[Cr(HCOO)$_3$] (Cr-HOIP) (*Pna*2$_1$ phase) perovskite formed a pseudo-cubic sub-lattice. Ghosh et al. [112] found that the magnetic spin configuration of this sub-lattice transforms from AFM-A to AFM-G and then to AFM-C (AFM = antiferromagnetic) when the compressive strain increased from 0 to 4%. The shrinking Cr–O bonds and Cr···Cr distances are responsible for the enhancement of the in-plane antiferromagnetic interactions. Under tensile stress, Cr–O bonds in Cr-HOIP transformed into two equivalent ferrodistortive sub-lattices due to the Jahn-Teller distortion of CrO_6 polyhedra, for which one sub-lattice can transform to the other by rotating 90°. This arrangement of Cr–O bonds agreed well with the anti-ferrodistortive orbital ordering of the $3d_{3x^2-r^2}$ and $3d_{3y^2-r^2}$ orbitals, which gave rise to a ferromagnetic coupling in the *ab* plane but an anti-ferromagentic coupling along the *c*-axis (AFM-A). More significantly, the in-plane ferroelectric polarization ($P_{Cr\text{-}HOIP}$) of was found to increase by more than 300% (from −0.22 to −0.92 μC/cm^2) when the compressive strain increases from 0 to 4%, while the $P_{Cr\text{-}HOIP}$ rose first then reached stable with the tensile strain increasing. When decomposing $P_{Cr\text{-}HOIP}$ into different functional groups: A-site GUA amine polarization (P_A) and BX_3 framework polarization (P_{BX3}), the contribution from P_A exhibited dominance in $P_{Cr\text{-}HOIP}$ due to the strain-dependent canting angle of GUA cation dipoles which resulted in a nonzero dipole moment along *c*-axis (Fig. 18b). By contrast, P_{BX3} showed an efficient contribution at the −4% compressive strain. It is notable that A-site GUA cations were more sensitive than BX_3 frameworks to the applied compressive strain. The polarization tunability via simulated epitaxial strain also has been witnessed in (FA)[Mn(HCOO)$_3$], the compressive strain up to 4% increased the polarization by more than 100% which majorly caused by the tilting of FA, the BX_3 framework was more sensible to strain than the FA amine. The above studies highlight the vital importance of strain engineering which can be facilely utilized to tune the magnetic ordering and ferroelectric polarization in these multiferroic hybrid perovskites.

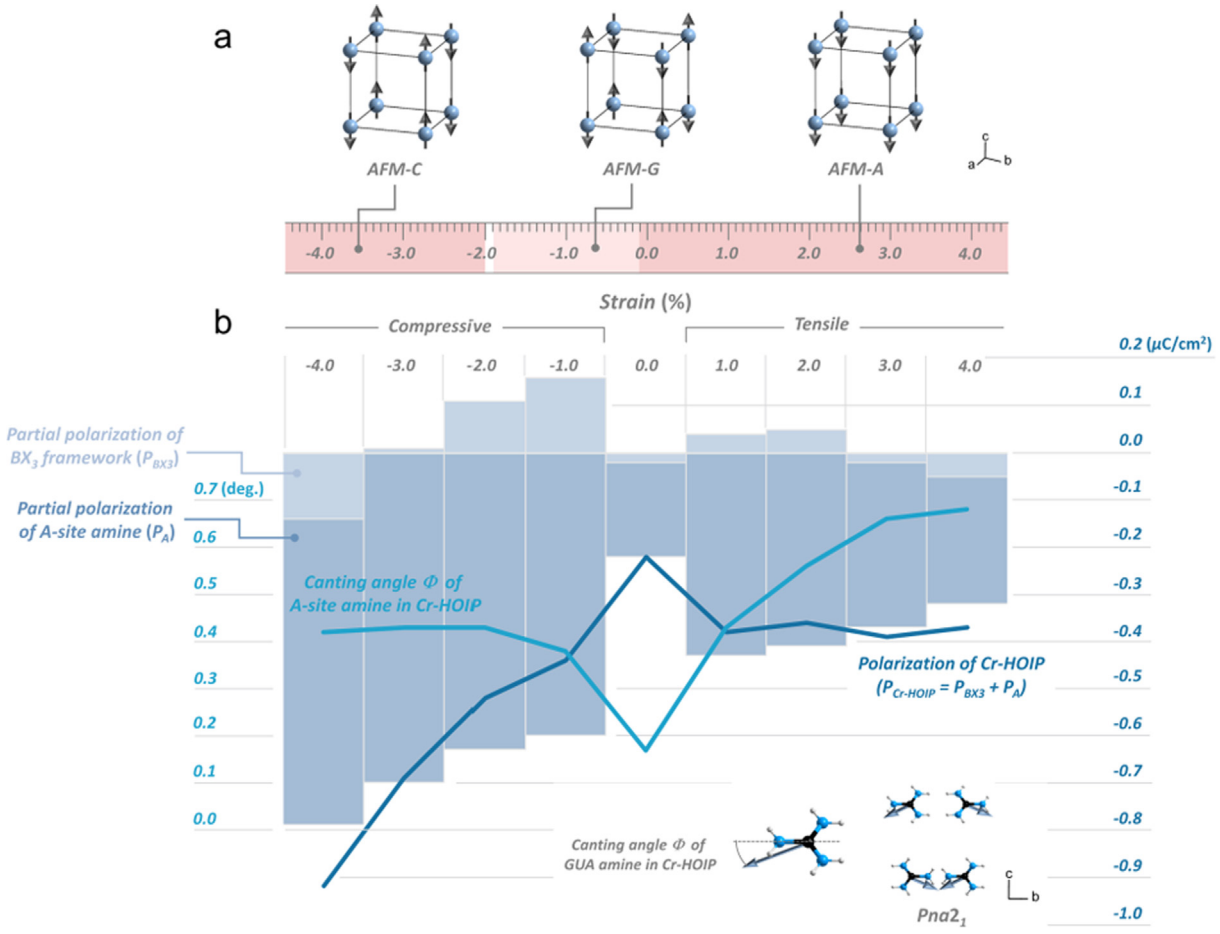

Fig. 18. (a) Strain dependence of magnetic spin configurations of Cr sub-lattice in (GUA)[Cr(HCOO)$_3$] (Cr-HOIP). The magnetic spin configurations such as ferromagnetic, and antiferromagnetic C-type (AFM-C), G-type (AFM-G) and A-type (AFM-A) were all taken into consideration to find out the lowest energy magnetic state for each strain state in *Pna*2$_1$ phase. (b) Total ($P_{Cr\text{-}HOIP}$) and partial polarization of A-site GUA amine (P_A) and BX_3 framework (P_{BX3}) for Cr-HOIP. The strain-dependent $P_{Cr\text{-}HOIP}$ (=P_A + P_{BX3}) was calculated under the lowest energy magnetic state of Cr sublattice. Inset: the canting angle Φ of the molecular dipole in A-site GUA amine in polar *Pna*2$_1$ phase. Φ was plotted as a function of strain. Figures are adapted with permission from Ref. [112], American Chemical Society.

6. Conclusion and outlook

The mechanical properties of HOIP materials with ABX_3 architectures are different from their oxide counterparts in two key ways: one is that the mechanical behavior of HOIPs can be tuned by the enormous diversity of organic molecules to achieve desirable assembly; the other way is that the additional degrees of freedom in the crystal structure enable HOIPs with significant mechanical flexibility. As been reviewed in this paper, abnormal anisotropic responses of halide HOIPs such as negative linear compressibility (NLC) and negative Poisson's ratios (NPRs) are predicted by first-principles calculations based on these two facts, however, experimental validation is critical and needs further investigation prior to proposing any kinds of applications. Furthermore, the rise of barocaloric effects from large entropy changes of phase transitions in HOIPs show potential applications for solid state cooling in comparison with traditionally used metallic and inorganic materials. On the other hand, more complex studies about the topics, for instance, how stress-strain in sub-lattice would regulate the intrinsic properties [113–123] of HOIP materials at the nanoscale is little known experimentally. Further investigations are required to promote the applications of HOIPs utilizing their pressure-induced property changes.

It was pointed out that there is a strong correlation between the stress-strain state and the intrinsic flexibility and stability of HOIP materials. Theoretical models have been proposed to simulate HOIP materials in the device-relevant forms, whilst an increasing number of experimental methods were developed to solve the performance loss due to strain effectively. These studies are benefiting the commercialization of HOIP materials, in particular, the perovskite solar cells. Overall, the exploration of HOIP mechanics is still in its infancy, and many challenges for HOIP applications suggest that their mechanical properties will continue to be a growing area of research which involves expertise in multidisplinary fields.

Acknowledgement

We acknowledge the financial support from the National Natural Science Foundation of China (No. 21571072) and the Fundamental Research Funds for the Central Universities (No. 63196006).

References

[1] S. Phillip, G. Brent, Science 358 (2017) 732–733.
[2] B. Saparov, D.B. Mitzi, Chem. Rev. 116 (2016) 4558–4596.
[3] W. Li, Z. Wang, F. Deschler, S. Gao, R.H. Friend, A.K. Cheetham, Nat. Rev. Mater. 2 (2017) 16099.
[4] D. Weber, Z. Naturforsch B 33 (1978) 1443–1445.
[5] Z. Wang, B. Zhang, T. Otsuka, K. Inoue, H. Kobayashi, M. Kurmood, Dalton Trans. (2004) 2209–2216.
[6] V.M. Golschmidt, Naturwissenschaften 49 (1926) 477–485.
[7] G. Kieslich, S. Sun, A.K. Cheetham, Chem. Sci. 5 (2014) 4712–4715.
[8] G. Kieslich, S. Sun, A.K. Cheetham, Chem. Sci. 6 (2015) 3430–3433.

[9] W. Travis, E.N.K. Glover, H. Bronstein, D.O. Scanlonbc, R.G. Palgrave, Chem. Sci. 7 (2016) 4548–4556.
[10] S. Burger, M.G. Ehrenreich, G. Kieslich, J. Mater. Chem. A 6 (2018) 21785–21793.
[11] G. Hodes, Science 342 (2013) 317–318.
[12] G. Feng, J. Ma, D. Gui, Z. Li, W. Li, Chin. J. Inorg. Chem. 33 (2017) 932–938.
[13] Q. Dong, J. Song, Y. Fang, Y. Shao, S. Ducharme, J. Huang, Adv. Mater. 28 (2016) 2816–2821.
[14] J.M. Bermúdez-García, M. Sánchez-Andújar, S. Castro-García, J. López-Beceiro, R. Artiaga, M.A. Señarís-Rodríguez, Nat. Commun. 8 (2017) 15715.
[15] N. Rolston, A.D. Printz, J.M. Tracy, H.C. Weerasinghe, D. Vak, L. Jia Haur, A. Priyadarshi, N. Mathews, D.J. Slotcavage, M.D. McGehee, R.E. Kalan, K. Zielinski, R.L. Grimm, H. Tsai, W. Nie, A.D. Mohite, S. Gholipour, M. Saliba, M. Grätzel, R.H. Dauskardt, Adv. Energy Mater. 8 (2018) 1702116.
[16] N. Rolston, K.A. Bush, A.D. Printz, A. Gold-Parker, Y. Ding, M.F. Toney, M.D. McGehee, R.H. Dauskardt, Adv. Energy Mater. 8 (2018) 1802139.
[17] C.C. Boyd, R. Cheacharoen, T. Leijtens, M.D. McGehee, Chem. Rev. (2018), https://doi.org/10.1021/acs.chemrev.8b00336.
[18] J. Feng, APL Mater. 2 (2014) 081801.
[19] S. Sun, F.H. Isikgor, Z. Deng, F. Wei, G. Kieslich, P.D. Bristowe, J. Ouyang, A.K. Cheetham, ChemSusChem 10 (2017) 3740–3745.
[20] Z. Deng, F. Wei, S. Sun, G. Kieslich, A.K. Cheetham, P.D. Bristowe, J. Mater. Chem. A 4 (2016) 12025–12029.
[21] S. Sun, Y. Fang, G. Kieslich, T.J. White, A.K. Cheetham, J. Mater. Chem. A 3 (2015) 18450–18455.
[22] Y. Rakita, S.R. Cohen, N.K. Kedem, G. Hodes, D. Cahen, MRS Commun. 5 (2015) 623–629.
[23] A.M. Lomonosov, X. Yan, C. Sheng, V.E. Gusev, C. Ni, Z. Shen, Phys. Status Solidi RRL 10 (2016) 606–612.
[24] A. Letoublon, S. Paofai, B. Ruffle, P. Bourges, B. Hehlen, T. Michel, C. Ecolivet, O. Durand, S. Cordier, C. Katan, J. Even, J. Phys. Chem. Lett. 7 (2016) 3776–3784.
[25] A.C. Ferreira, A. Létoublon, S. Paofai, S. Raymond, C. Ecolivet, B. Rufflé, S. Cordier, C. Katan, M.I. Saidaminov, A.A. Zhumekenov, O.M. Bakr, J. Even, P. Bourges, Phys. Rev. Lett. 121 (2018) 085502.
[26] P.A. Mante, C.C. Stoumpos, M.G. Kanatzidis, A. Yartsev, J. Phys. Chem. Lett. 9 (2018) 3161–3166.
[27] S. Chen, R. Shang, K.-L. Hu, Z.-M. Wang, S. Gao, Inorg. Chem. Front. 1 (2014) 83–98.
[28] R. Shang, G.C. Xu, Z.M. Wang, S. Gao, Chem. Eur. J. 20 (2014) 1146–1158.
[29] I.E. Collings, J.A. Hill, A.B. Cairns, R.I. Cooper, A.L. Thompson, J.E. Parker, C.C. Tang, A.L. Goodwin, Dalton Trans. 45 (2016) 4169–4178.
[30] S. Varughese, M.S. Kiran, U. Ramamurty, G.R. Desiraju, Angew. Chem. Int. Ed. 52 (2013) 2701–2712.
[31] A. Jaffe, Y. Lin, C.M. Beavers, J. Voss, W.L. Mao, H.I. Karunadasa, ACS Cent. Sci. 2 (2016) 201–209.
[32] M. Faghihnasiri, M. Izadifard, M.E. Ghazi, J. Phys. Chem. C 121 (2017) 27059–27070.
[33] L. Dong, S. Sun, Z. Deng, W. Li, F. Wei, Y. Qi, Y. Li, X. Li, P. Lu, U. Ramamurty, Comput. Mater. Sci. 141 (2018) 49–58.
[34] J.-H. Lee, Z. Deng, N.C. Bristowe, P.D. Bristowe, A.K. Cheetham, J. Mater. Chem. C 6 (2018) 12252–12259.
[35] R. Ferencz, J. Sanchez, B. Blümich, W. Herrmann, Polym. Test. 31 (2012) 425–432.
[36] L.-J. Ji, S.-J. Sun, Y. Qin, K. Wang, W. Li, Unpublished results.
[37] S. Ryu, H. Kim, H.J. Kim, S. Kim, J. Ceram. Soc. Jpn. 117 (2009) 811–814.
[38] M.A. Ramírez, R. Parra, M.M. Reboredo, J.A. Varela, M.S. Castro, L. Ramajo, Mater. Lett. 64 (2010) 1226–1228.
[39] N.C. Burtch, J. Heinen, T.D. Bennett, D. Dubbeldam, M.D. Allendorf, Adv. Mater. 30 (2018) 1704124.
[40] Y. Wang, X. Lu, W. Yang, T. Wen, L. Yang, X. Ren, L. Wang, Z. Lin, Y. Zhao, J. Am. Chem. Soc. 137 (2015) 11144–11149.
[41] W. Li, A. Thirumurugan, P.T. Barton, Z. Lin, S. Henke, H.H. Yeung, M.T. Wharmby, E.G. Bithell, C.J. Howard, A.K. Cheetham, J. Am. Chem. Soc. 136 (2014) 7801–7804.
[42] D. Gui, L. Ji, A. Muhammad, W. Li, W. Cai, Y. Li, X. Li, X. Wu, P. Lu, J. Phys. Chem. Lett. 9 (2018) 751–755.
[43] J.C. Tan, P. Jain, A.K. Cheetham, Dalton Trans. 41 (2012) 3949–3952.
[44] G. Feng, D. Gui, W. Li, Cryst. Growth Des. 18 (2018) 4890–4895.
[45] G. Giorgi, J.-I. Fujisawa, H. Segawa, K. Yamashita, J. Phys. Chem. C 118 (2014) 12176–12183.
[46] H. John, Inorganic Chemistry Principles of Structure and Re Activity, fourth ed., HarperCollins College, 1993, p. 1993.
[47] F. Wei, Z. Deng, S. Sun, F. Zhang, D.M. Evans, G. Kieslich, S. Tominaka, M.A. Carpenter, J. Zhang, P.D. Bristowe, A.K. Cheetham, Chem. Mater. 29 (2017) 1089–1094.
[48] M.A. Reyes-Martinez, A.L. Abdelhady, M.I. Saidaminov, D.Y. Chung, O.M. Bakr, M.G. Kanatzidis, W.O. Soboyejo, Y.L. Loo, Adv. Mater. 29 (2017) 1606556.
[49] Y. Wu, S. Shaker, F. Brivio, R. Murugavel, P.D. Bristowe, A.K. Cheetham, J. Am. Chem. Soc. 139 (2017) 16999–17002.
[50] Y. Wu, T. Binford, J.A. Hill, S. Shaker, J. Wang, A.K. Cheetham, Chem. Commun. 54 (2018) 3751–3754.
[51] Q. Zeng, K. Wang, B. Zou, ACS Appl. Mater. Interfaces 10 (2018) 23481–23484.
[52] X. Lu, W. Yang, Q. Jia, H. Xu, Chem. Sci. 8 (2017) 6764–6776.
[53] I.P. Swainson, M.G. Tucker, D.J. Wilson, B. Winkler, V. Milman, Chem. Mater. 19 (2007) 2401–2405.
[54] L. Wang, K. Wang, B. Zou, J. Phys. Chem. Lett. 7 (2016) 2556–2562.
[55] L. Wang, K. Wang, G. Xiao, Q. Zeng, B. Zou, J. Phys. Chem. Lett. 7 (2016) 5273–5279.
[56] T. Yin, Y. Fang, W.K. Chong, K.T. Ming, S. Jiang, X. Li, J.L. Kuo, J. Fang, T.C. Sum, T.J. White, J. Yan, Z.X. Shen, Adv. Mater. 30 (2018) 1705017.
[57] L. Wang, T. Ou, K. Wang, G. Xiao, C. Gao, B. Zou, Appl. Phys. Lett. 111 (2017) 233901.
[58] M. Szafranski, A. Katrusiak, J. Phys. Chem. Lett. 7 (2016) 3458–3466.
[59] S. Jiang, Y. Luan, J.I. Jang, T. Baikie, X. Huang, R. Li, F.O. Saouma, Z. Wang, T.J. White, J. Fang, J. Am. Chem. Soc. 140 (2018) 13952–13957.
[60] S. Jiang, Y. Fang, R. Li, H. Xiao, J. Crowley, C. Wang, T.J. White, W.A. Goddard III, Z. Wang, T. Baikie, J. Fang, Angew. Chem. Int. Ed. 55 (2016) 6540–6544.
[61] T. Ou, J. Yan, C. Xiao, W. Shen, C. Liu, X. Liu, Y. Han, Y. Ma, C. Gao, Nanoscale 8 (2016) 11426–11431.
[62] X. Lu, Y. Wang, C.C. Stoumpos, Q. Hu, X. Guo, H. Chen, L. Yang, J.S. Smith, W. Yang, Y. Zhao, H. Xu, M.G. Kanatzidis, Q. Jia, Adv. Mater. 28 (2016) 8663–8668.
[63] L. Kong, G. Liu, J. Gong, Q. Hu, R.D. Schaller, P. Dera, D. Zhang, Z. Liu, W. Yang, K. Zhu, Y. Tang, C. Wang, S.H. Wei, T. Xu, H.K. Mao, Proc. Natl. Acad. Sci. USA 113 (2016) 8910–8915.
[64] G. Liu, L. Kong, J. Gong, W. Yang, H.-K. Mao, Q. Hu, Z. Liu, R.D. Schaller, D. Zhang, T. Xu, Adv. Funct. Mater. 27 (2017) 1604208.
[65] T. Wang, B. Daiber, J.M. Frost, S.A. Mann, E.C. Garnett, A. Walsh, B. Ehrler, Energ. Environ. Sci. 10 (2017) 509–515.
[66] C.W. Huang, W. Ren, V.C. Nguyen, Z. Chen, J. Wang, T. Sritharan, L. Chen, Adv. Mater. 24 (2012) 4170–4174.
[67] N. Listed, Nat. Mater. 10 (2011) 807.
[68] F. Coudert, J.D. Evans, Coordin, Chem. Rev. 388 (2019) 48–62.
[69] R.H. Baughman, J.M. Shacklette, A.A. Zakhidov, S. Stafstrom, Nature 392 (1998) 362–364.
[70] K.E. Evans, A. Alderson, Adv. Mater. 12 (2000) 617–628.
[71] G.N. Greaves, A.L. Greer, R.S. Lakes, T. Rouxel, Nat. Mater. 10 (2011) 823–837.
[72] N.R. Keskar, J.R. Chelikowsky, Nature 358 (1992) 222–224.
[73] R. Lakes, Science 235 (1987) 1038–1040.
[74] J.N. Grima, R. Jackson, A. Alderson, K.E. Evans, Adv. Mater. 12 (2000) 1912–1917.
[75] K. Bertoldi, P.M. Reis, S. Willshaw, T. Mullin, Adv. Mater. 22 (2010) 361–366.
[76] L. Dong, D.S. Stone, R.S. Lakes, Philos. Mag. Lett. 90 (2010) 23–33.
[77] C.W. Smith, R.J. Wootton, K.E. Evans, Exp. Mech. 39 (1999) 356–362.
[78] W. Li, M.R. Probert, M. Kosa, T.D. Bennett, A. Thirumurugan, R.P. Burwood, M. Parinello, J.A. Howard, A.K. Cheetham, J. Am. Chem. Soc. 134 (2012) (1943) 11940–11941.
[79] A. Marmier, Z.A.D. Lethbridge, R.I. Walton, C.W. Smith, S.C. Parker, K.E. Evans, Comput. Phys. Commun. 181 (2010) 2102–2115.
[80] A.B. Cairns, A.L. Goodwin, Phys. Chem. Chem. Phys. 17 (2015) 20449–20465.
[81] S.I. Ranganathan, M. Ostoja-Starzewski, Phys. Rev. Lett. 101 (2008) 055504.
[82] J.N. Grima, R. Gatt, A. Alderson, K.E. Evans, J. Mater. Chem. 15 (2005) 4003–4005.
[83] C. Huang, L. Chen, Adv. Mater. 28 (2016) 8079–8096.
[84] J.J. Williams, C.W. Smith, K.E. Evans, Chem. Mater. 19 (2007) 2423–2434.
[85] L. Mañosa, A. Planes, M. Acet, J. Mater. Chem. A 1 (2013) 4925–4936.
[86] K. Alex Müller, F. Fauth, S. Fischer, M. Koch, A. Furrer, P. Lacorre, Appl. Phys. Lett. 73 (1998) 1056–1058.
[87] T. Strässle, A. Furrer, High Pressure Res. 17 (2000) 325–333.
[88] L. Manosa, D. Gonzalez-Alonso, A. Planes, E. Bonnot, M. Barrio, J.L. Tamarit, S. Aksoy, M. Acet, Nat. Mater. 9 (2010) 478–481.
[89] X. Moya, S. Kar-Narayan, N.D. Mathur, Nat. Mater. 13 (2014) 439–450.
[90] J.M. Bermudez-Garcia, M. Sanchez-Andujar, S. Yanez-Vilar, S. Castro-Garcia, R. Artiaga, J. Lopez-Beceiro, L. Botana, A. Alegria, M.A. Senaris-Rodriguez, Inorg. Chem. 54 (2015) 11680–11687.
[91] C.N.R. Rao, K.J. Rao, Phase Transitions in Solids, McGraw Hill, 1978.
[92] M. Szafrański, W.-J. Wei, Z.-M. Wang, W. Li, A. Katrusiak, APL Mater. 6 (2018) 100701.
[93] A. Rorrin, A. Ienco, F. Costantino, T. Montini, B.D. Credico, M. Caporali, L. Gonsalvi, P. Fornasiero, M. Peruzzini, Cryst. Growth Des. 8 (2008) 3302–3308.
[94] R.B. Griffiths, Phys. Rev. Lett. 24 (1970) 715–717.
[95] J.M. Bermúdez-García, S. Yáñez-Vilar, A. García-Fernández, M. Sánchez-Andújar, S. Castro-García, J. López-Beceiro, R. Artiaga, M. Dilshad, X. Moya, M.A. Señarís-Rodríguez, J. Mater. Chem. C 6 (2018) 9867–9874.
[96] S. Chen, G. Shi, Adv. Mater. 29 (2017) 1605448.
[97] M. Ptak, M. Mączka, A. Gągor, A. Sieradzki, A. Stroppa, D. Di Sante, J.M. Perez-Mato, L. Macalik, Dalton Trans. 45 (2016) 2574–2583.
[98] S. Liu, R.E. Cohen, J. Phys. Chem. C 120 (2016) 17274–17281.
[99] K.P. Ong, T.W. Goh, Q. Xu, A. Huan, J. Phys. Chem. C 6 (2015) 681–685.
[100] J. Berry, T. Buonassisi, D.A. Egger, G. Hodes, L. Kronik, Y.L. Loo, I. Lubomirsky, S.R. Marder, Y. Mastai, J.S. Miller, D.B. Mitzi, Y. Paz, A.M. Rappe, I. Riess, B. Rybtchinski, O. Stafsudd, V. Stevanovic, M.F. Toney, D. Zitoun, A. Kahn, D. Ginley, D. Cahen, Adv. Mater. 27 (2015) 5102–5112.
[101] J. Zhao, Y. Deng, H. Wei, X. Zheng, Z. Yu, Y. Shao, J.E. Shield, J. Huang, Sci. Adv. 3 (2017) eaao5616.
[102] A. Basu, P. Kour, S. Parmar, R. Naphade, S. Ogale, J. Phys. Chem. C 122 (2018) 4802–4808.
[103] C. Ramirez, S.K. Yadavalli, H.F. Garces, Y.Y. Zhou, N.P. Padture, Scr. Mater. 150 (2018) 36–41.
[104] N. Rolston, B.L. Watson, C.D. Bailie, M.D. McGehee, J.P. Bastos, R. Gehlhaar, J.-E. Kim, D. Vak, A.T. Mallajosyula, G. Gupta, A.D. Mohite, R.H. Dauskardt, Extreme Mech. Lett. 9 (2016) 353–358.

[105] M. Park, H.J. Kim, I. Jeong, J. Lee, H. Lee, H.J. Son, D.-E. Kim, M.J. Ko, Adv. Energy Mater. 5 (2015) 1501406.
[106] J. Yu, M. Wang, S. Lin, ACS Nano 10 (2016) 11044–11057.
[107] K.A. Bush, N. Rolston, A. Gold-Parker, S. Manzoor, J. Hausele, Z.J. Yu, J.A. Raiford, R. Cheacharoen, Z.C. Holman, M.F. Toney, R.H. Dauskardt, M.D. McGehee, ACS Energy Lett. 3 (2018) 1225–1232.
[108] X. Zheng, C. Wu, S.K. Jha, Z. Li, K. Zhu, S. Priya, ACS Energy Lett. 1 (2016) 1014–1020.
[109] M. Spina, A. Karimi, W. Andreoni, C.A. Pignedoli, B. Náfrádi, L. Forró, E. Horváth, Appl. Phys. Lett. 110 (2017) 121903.
[110] J. Liu, Y. Xue, Z. Wang, Z. Xu, C. Zheng, B. Weber, J. Song, Y. Wang, Y. Lu, Y. Zhang, Q. Bao, ACS Nano 10 (2016) 3536–3542.
[111] Q. Tu, I. Spanopoulos, S. Hao, C. Wolverton, M.G. Kanatzidis, G.S. Shekhawat, V.P. Dravid, ACS Appl. Mater. Interfaces 10 (2018) 22167–22173.
[112] S. Ghosh, D. Di Sante, A. Stroppa, J. Phys. Chem. Lett. 6 (2015) 4553–4559.
[113] F. Fan, H. Wu, D. Nabok, S. Hu, W. Ren, C. Draxl, A. Stroppa, J. Am. Chem. Soc. 139 (2017) 12883–12886.
[114] D. Di Sante, A. Stroppa, P. Jain, S. Picozzi, J. Am. Chem. Soc. 135 (2013) 18126–18130.
[115] A. Stroppa, P. Jain, P. Barone, M. Marsman, J.M. Perez-Mato, A.K. Cheetham, H. W. Kroto, S. Picozzi, Angew. Chem. Int. Ed. 50 (2011) 5847–5850.
[116] P. Jain, A. Stroppa, D. Nabok, A. Marino, A. Rubano, D. Paparo, M. Matsubara, H. Nakotte, M. Fiebig, S. Picozzi, E.S. Choi, A.K. Cheetham, C. Draxl, N.S. Dalal, V.S. Zapf, Npj Quantum Mater. 1 (2016) 16012.
[117] Y. Tian, A. Stroppa, Y. Chai, L. Yan, S. Wang, P. Barone, S. Picozzi, Y. Sun, Sci. Rep. 4 (2014) 6062.
[118] A. Stroppa, D. Di Sante, P. Barone, M. Bokdam, G. Kresse, C. Franchini, M. Whangbo, S. Picozzi, Nat. Commun. 5 (2014) 5900.
[119] L.C. Gomez-Aguirre, B. Pato-Doldan, A. Stroppa, S. Yanez-Vilar, L. Bayarjargal, B. Winkler, S. Castro-Garcia, J. Mira, M. Sanchez-Andujar, M.A. Senaris-Rodriguez, Inorg. Chem. 54 (2015) 2109–2116.
[120] Y. Tian, A. Stroppa, Y. Chai, P. Barone, M. Perez-Mato, S. Picozzi, Y. Sun, Phys. Status Solidi RRL 9 (2015) 62–67.
[121] L. Mazzuca, L. Canadillas-Delgado, J.A. Rodriguez-Velamazan, O. Fabelo, M. Scarrozza, A. Stroppa, S. Picozzi, J. Zhao, X. Bu, J. Rodriguez-Carvajal, Inorg. Chem. 56 (2017) 197–207.
[122] M.E. Kamminga, A. Stroppa, S. Picozzi, M. Chislov, I.A. Zvereva, J. Baas, A. Meetsma, G.R. Blake, T.T.M. Palstra, Inorg. Chem. 56 (2017) 33–41.
[123] W. Zhao, C. Shi, A. Stroppa, D. Di Sante, F. Cimpoesu, W. Zhang, Inorg. Chem. 55 (2016) 10337–10342.